MASS SPECTROMETRIC STUDIES OF IONIZATION IN SHOCK HEATED GAS MIXTURES

Thesis by

Charles C. P. Wang

In Partial Fulfillment of the Requirements

For the Degree of

Doctor of Philosophy

California Institute of Technology

Pasadena, California

1967

(Submitted May 2, 1967)

ACKNOWLEDGMENT

The author wishes to express his appreciation to Professor B. Sturtevant, who introduced him to this field of study and under whose direction the research was carried out. Thanks are due also to Professor H. W. Liepmann whose interest and encouragement helped to make this thesis possible. The generous help of A. Hoffman, who painstakingly corrected the English, the other members of the staff of the Graduate Aeronautical Laboratories, who helped with the experiment, and Misses H. Burrus and M. Fossum, who typed the manuscript, is also gratefully acknowledged.

The author is indebted to the California Institute of Technology for various forms of financial assistance. The research was partially supported by the National Aeronautics and Space Administration.

Finally, the deepest appreciation of all is felt for his wife, Lily, for her patience and encouragement during these years of graduate work.

ABSTRACT

The initial stage of thermal ionization in gas mixtures behind strong normal shock waves has been studied using a mass spectrometer. The sampling process, the unique role of mass spectrometric analysis, the ionization mechanism and the effect of impurities on the ionization relaxation time of the inert gases are discussed. A detailed analysis of ion diffusion through the end wall thermal boundary layer to investigate the effect of the sampling process on the reaction and reaction products are described. The experiments were conducted in argon and xenon at temperatures of from 10,000 ^{o}K to 30,000 ^{o}K and pressures from 15 mmHg to 80 mmHg. A large number of different ions were detected in "pure" (the estimated level of naturally occurring impurities was 50 ppm) argon. H^{+} and O^{+} were found in much greater amounts than any of the other products. The roles of H and O were studied further by mixing a small amount of H_2 or O_2 in argon. The activation energy and the effective cross section for ionization were obtained from the measured ionization rate. For argon, the activation energy agrees within experimental accuracy with the result of Kelly (1966). For hydrogen the activation energy is about 10 ev, and this value coincides with its first excited state. The effective cross section is a thousand times larger than the corresponding effective cross section for the ionization of argon. This explains why small amounts of hydrogen affect the argon ionization relaxation time.

TABLE OF CONTENTS

TABLE OF CONTENTS (Cont.)

LIST OF TABLES

LIST OF FIGURES

I. INTRODUCTION

In the study of gas dynamics, when a gas is suddenly heated by a shock wave and begins to ionize, the ionization relaxation process becomes important in determining the thermal and transport properties of the gas and the extent of the relaxation region behind the shock wave. During the past ten years, the ionization relaxation process in a shock heated inert gas has been studied in detail by many investigators (Petschek and Byron (1957), Weymann (1958), Sturtevant (1961), Harwell and Jahn (1964), Kelly (1966) etc.).

Petschek and Byron found that the ionization of argon can be approximately divided into two stages: the initial ionization by inherently slow inelastic atom-atom collisional processes, and final rapid approach to equilibrium by relatively efficeint electron-atom collisional processes. Therefore, the relaxation time (or ionization time) is determined by the ionization kinetics of the initial stage of the relaxation process. A remarkable result was also noted in that the relaxation time depends strongly on the presence of impurities* even after considerable care is taken to insure high purity (impurity level from 7 ppm to 80 ppm).

Weymann postulated a two-step process for the initial stage of ionization in inert gases; the excitation of an atom to the resonance state followed by ionization of the excited atom. He also assumed that the collision cross sections (defined in section 2.1) of excitation

---

* The major source of impurities in most experiments is leakage and degassing into the shock tube after introduction of the test gas.

(from ground state to an excited electronic state) and ionization (from an excited electronic state to ionization) are about the same. These lead to the results: a) the activation energy (defined in section 2.1) for the ionization process is the ionization energy, b) this two-step process is more efficient than the one-step ionization process, and c) influence of the impurities on the argon ionization rate is negligible as long as the impurity concentration is below about 10^3 ppm.

Sturtevant has studied the ionization of argon by measuring the effusive electrical current through a small orifice in the end wall of a shock tube. He has shown that the initial stage of ionization results from a complicated series of consecutive reactions.

Harwell and Jahn, and Kelly have studied the ionization of shock heated inert gases by using a transverse microwave probe. They found that the effective activation energy for ionizing argon coincides within experimental error with the excitation energy of the first electronic excited state rather than with the ionization energy, indicating that the initial stage of ionization does proceed via two-step process as proposed by Weymann but that the excitation step is rate controlling. They also found, as did Petschek and Byron, that unknown impurities in the test gases have profound effects on the ionization rates at concentrations as low as a few parts per million.

Little is known about the initial atom-atom ionization process because of both the complexity of the theory of the interaction between colliding atomic particles and the extreme difficulties encountered in experimental studies with low-energy molecular beams. Theoretical calculations, except in the simplest cases, have rarely been attempted

at low energies, and the experimental data is sparse and discrepant.

The main interest of the present study is a) to study the initial atom-atom ionization process, b) to discover what impurities, in such small concentrations, can have so important an effect on the rate of ionization, and c) to determine the means by which they exert this influence. The mass spectrometer, with its unique ability to identify ions of different masses, seems to be an ideal instrument for this study. The predominant impurity ions can be found and their behavior can be studied individually. One of the inherent problems encountered in using a mass spectrometer is the analysis of the sampling process. This involves the extraction of a sample of ions from the relaxation region behind the shock wave and the measurement of its composition and magnitude subsequent to its removal from the shock tube. Because of the variety and difficulty of the problems associated with the thermal layer (section 4. 1) formed near the sampling orifice, and reactions within it, it is difficult to make any general analysis about sampling. However, a simple analysis with a few basic assumptions is made to demonstrate the essential features of the sampling process.

In this study the GALCIT* 17-inch shock tube is used to produce the shock wave and a modified Nier type magnetic mass spectrometer is used to study the ionization. A theoretical model of the initial ionization process is also proposed to interpret the experimental results.

---

* Graduate Aeronautical Laboratories, California Institute of Technology.

II. KINETICS OF THE INITIAL IONIZATION PROCESS

The initial stage of ionization in a shock heated inert gas is governed by atom-atom* inelastic collisions. A description of the inelastic collision process, the rate equations, and various models of the ionization process are given in the following section.

2.1 Inelastic Collision Processes

An inelastic collision process is an interaction between two atoms (or molecules) that involves the exchange of kinetic energy and internal energy. The internal energy includes rotational and vibrational energy, plus the energies of dissociation and ionization etc. For monatomic gases, the internal energies are only the energies of electronic excitation and ionization.

For the temperatures and pressures of interest in these experiments, the atom can be considered as a classical particle (the requirement is that the average de Broglie wave length of an atom is much smaller than the average interparticle separation) and the collisions are binary collisions.

Considering the binary collision, let the velocities of the two incoming particles be $\underline{v}_1$, $\underline{u}_2$, their mases be m_1, m_2 and their velocity distribution functions be $f_1(\underline{v}_1, t)$, and $f_2(\underline{v}_2, t)$ (assuming homogeneity in space). Regard particles denoted by $(\ )_2$ as a beam with velocity $\underline{v}_2$ incident on the particles of velocity $\underline{v}_1$. The flux of this incident beam is

---

* For the initial stage of ionization the electron density is low enough so that both the electron-atom ionization and electron-ion recombination can be neglected.

$$I(\underline{v}_1, \underline{v}_2)d\underline{v}_2 = f_2(\underline{v}_2, t)\left|\underline{v}_1 - \underline{v}_2\right| \; d\underline{v}_2. \tag{1}$$

Define the collision cross section S of the reaction as

$$S(\left|\underline{v}_2 - \underline{v}_1\right|) = \frac{\text{Number of reactions per unit time/particle}}{\text{Incident flux}} \tag{2}$$

The collision frequency or the number of reactions per second is then

$$\frac{dn^*}{dt} = \int\int I\, S\, f_1(\underline{v}_1, t)d\underline{v}_2 \; d\underline{v}_1$$

$$= \int\int f_1(\underline{v}_1, t)f_2(\underline{v}_2, t)S(\; \underline{v}_2 - \underline{v}_1 \;)\left|\underline{v}_2 - \underline{v}_1\right| \; d\underline{v}_2 d\underline{v}_1. \tag{3}$$

If it is assumed that the reaction rate is slow enough that the distribution function f is not disturbed from Maxwellian during the reaction, i. e.

$$f(v) = n\left(\frac{m}{2\pi kT}\right)^{3/2} \exp\left(-\frac{mv^2}{2kT}\right), \tag{4}$$

and that the temperatures of the two species are equal,

$$T_1 = T_2 = T, \tag{5}$$

then

$$\frac{dn^*}{dt} = \frac{1}{2} n_1 n_2 \frac{(m_1 m_2)^{3/2}}{(2\pi kT)^3} \int\int \exp\left(-\frac{m_1 v_1^2}{2kT} - \frac{m_2 v_2^2}{2kT}\right) S(\; \underline{v}_2 - \underline{v}_1 \;)\left|\underline{v}_2 - \underline{v}_1\right| d\underline{v}_2 d\underline{v}_1 \tag{6}$$

These are well justified assumptions for atom-atom collisional processes.

To uncouple the above integrals a transformation is made from laboratory coordinates to center of mass coordinates. Let the total mass M, the reduced mass μ, the mass center velocity $\underline{V}$, and the relative velocity $\underline{g}$ be, respectively

$$\begin{aligned} M &= m_1 + m_2 \\ \mu &= \frac{m_1 m_2}{m_1+m_2} \\ \underline{V} &= \frac{m_1\underline{v}_1+m_2\underline{v}_2}{M} \\ \underline{g} &= \underline{v}_1 - \underline{v}_2 \end{aligned} \tag{7}$$

Then the total energy E of the system is equal to the center of mass energy E_c plus the relative energy E_r. That is

$$E = \frac{1}{2} m_1 v_1^2 + \frac{1}{2} m_2 v_2^2 = E_c + E_r \tag{8}$$

where $E_c = \frac{1}{2} M V^2$ and $E_r = \frac{1}{2}\mu g^2$. Furthermore, the Jacobian,

$$J\left(\begin{matrix}\underline{v}_1, \underline{v}_2 \\ \underline{V}, \underline{g}\end{matrix}\right) = 1$$

that is, $d\underline{v}_1\, d\underline{v}_2 = d\underline{V}\, d\underline{g}$.

Therefore (Chapman and Cowling, 1952):

$$\frac{dn^*}{dt} = \frac{1}{2} n_1 n_2 \frac{(m_1 m_2)^{3/2}}{(2\pi kT)^3} \int_{-\infty}^{\infty} \exp\left(-\frac{MV^2}{2kT}\right) d\underline{V} \int_{-\infty}^{\infty} \exp\left(-\frac{\mu g^2}{2kT}\right) S(g) g\, d\underline{g} \tag{9}$$

If the reaction requires a minimum energy transfer E^*, then $S(g)$ can be written as $S^*(g)\, H(E_r - E^*)$, where H is the Heaviside unit function, and

$$\frac{dn^*}{dt} = \frac{1}{16}\, n_1 n_2\, \frac{(m_1 m_2)^{3/2}}{(2\pi kT)^{3/2}} \int_{g > g_o} \exp\left(-\frac{\mu g^2}{2kT}\right) S^*(g) g\, d\underline{g} \qquad (10)$$

where $g_o = \left(\frac{2E^*}{\mu}\right)^{1/2}$.

Experimental or theoretical data regarding the cross section $S^*(g)$ for ionization or excitation processes are scarce. In the initial ionization of argon, Weymann (1958) assumed that $S^*(g)$ is a constant to simplify the calculations. Later Harwell and Jahn (1964) assumed that $S^*(g)$ increases linearly with the excess relative energy $(E_r - E^*)$. Fortunately, our main interest, the reaction rate, depends on the integral of the cross section weighted by the Boltzman factor (equation 10), and is not strongly dependent on the functional form of $S^*(g)$ at temperatures of interest here. However, for generality, it is assumed that $S^*(g)$ is proportional to the nth power of the excess relative energy, that is,

$$S^*(g) = (E_r - E^*)^n\, S_n^* \qquad (11)$$

Equation (10) then becomes

$$\frac{dn^*}{dt} = n_1 n_2 \left(\frac{2kT}{\mu\pi}\right)^{1/2} S_n^*\, (kT)^n \left(\frac{E^*}{kT} + \frac{(n+1)!}{n!}\right) \exp\left(-\frac{E^*}{kT}\right). \qquad (12)$$

In this expression, there are three constant parameters E^*, S_n^* and n to be determined by experiment. From the measured rates, $\frac{dn^*}{dt}$, at different temperatures, these parameters can be determined by an Arrhenius plot of $\frac{dn^*}{dt}$ against 1/kT.

Now, in chemical kinetics the bimolecular reaction of second order can be written as (Benson, 1960)

$$\frac{dn^*}{dt} = k^* n_1 n_2$$

The rate constant, k^*, is most conveniently expressed empirically as $Ae^{-E^*/kT}$ (Arrhenius form), where A is called the pre-exponential factor and E^* is called the activation energy. The validity and the physical meaning of this empirical form is demonstrated by the above consideration of binary inelastic collisions.

2.2 Ionization Rates in Pure Gases

Atom-atom ionization is a very complicated process. It depends on the electron energy states of each atom, the interaction potentials between atoms, the relative energy of the particles, the collision parameters, etc. To demonstrate the essential features a few simple models are analyzed for the reaction.

a) The simplest model for ionization is the one-step process, which assumes that ionization may be achieved by one energetic collision. That is:

$$A + A \xrightarrow{k^+} A + A^+ + e. \qquad (13)$$

The rate equation can be written as

$$\frac{dn_A^+}{dt} = k^+(T) n_A^2 \ , \tag{14}$$

where $k^+(T)$ is the ionization rate constant. In this case the activation energy, E^*, is just the ionization energy E^+, and the collision cross section, S_n^*, is just the ionization collision cross section S_n^+. From equation (12) the rate constant can be written as

$$k^+(T) = \left(\frac{2kT}{\mu\pi}\right)^{1/2} S_n^+ (kT)^n \left(\frac{E^+}{kT} + \frac{(n+1)!}{n!}\right) \exp\left(-\frac{E^+}{kT}\right). \tag{15}$$

The main feature of this reaction is that n_A^+ increases linearly with time (figure 1) until electron-atom ionization becomes important.

b) The two-step ionization process assumed that ionization may be achieved by two successive collisions, involving an intermediate excited state A^*. That is,

$$\begin{aligned} A + A &\underset{\longleftarrow}{\xrightarrow{k^*}} A^* + A \\ A + A^* &\xrightarrow{k^+} A^+ + A + e \\ A^* &\underset{\longleftarrow}{\xrightarrow{\overline{k}_\nu}} A + h\nu \ . \end{aligned} \tag{16}$$

Then the rate equations are

$$\frac{dn_A^*}{dt} = k^* n_A^2 - (k^+ + k') n_A n_A^* - k_\nu n_A^* \qquad (17)$$

$$\frac{dn_A^+}{dt} = k^+ n_A n_A^*$$

where $k^*(T)$ = excitation rate constant

E_A^* = excitation energy

S^* = excitation cross section

k^+ = ionization rate constant

k' = de-excitation rate constant

k_ν = effective radiative decay rate.

After integrating:

$$n_A^* = k^* n_A^2 \tau \, (1-e^{-t/\tau})$$

$$n_A^+ = k^* k^+ \tau \, n_A^3 \, [t - \tau (1-e^{-t/\tau})] \qquad (18)$$

where $\tau = [(k^+ + k')n_A + k_\nu]^{-1}$.

The efficiency of this process, as compared with a one-step process, depends on the relative rates of collisional de-excitation (k') and radiative decay (k_ν) to the ionization step (k^+). The natural lifetime of a normal excited state with respect to radiative decay ($\sim 10^{-8}$ sec) is probably inadequate to support this process. However, Harwell and Jahn (1964) have demonstrated that, due to either the resonance trapping mechanism (Weymann 1958, Phelps 1958) or the fact that the excited state A^* is a long-lived metastable state

(Appendix B), the effective lifetimes of the excited states with respect to radiative decay and collisional de-excitation are sufficiently long to permit a second ionization collision. Thus, assuming $k_\nu << (k^+ + k')n_A$,

$$n_A^* = \frac{k^* n_A}{(k^+ + k')} (1 - e^{-t/\tau}), \tag{19}$$

$$n_A^+ = \frac{k^* k^+}{k^+ + k'} n_A^2 \left[t - \tau (1 - e^{-t/\tau})\right],$$

where $\tau = \left[(k^+ + k')n_A\right]^{-1}$.

For small time, $t << \tau$,

$$n_A^+ \simeq \frac{1}{2} k^* k^+ n_A^3 t^2 \tag{20}$$

and for large time, $t >> \tau$,

$$n_A^+ \simeq \frac{k^* k^+}{k^+ + k'} n_A^2 t$$

Therefore, during the transients in which the population of the excited state increases to its "steady-state" value, n_A^+ increases with the square of the time, after which it increases linearly (figure 1). Hence, for large time, this two-step ionization process is more efficient than the one-step ionization process. That is, the two-step ionization process can be considered as equivalent to a one-step ionization process with an effective rate constant $k^* k^+/(k^+ + k')$. Physically, this means that once the atom is excited it will eventually become ionized.

c) Extending the idea of a two-step process, the multi-step ionization process assumes that ionization may be achieved by one or

more successive collisions after the atom has been excited to the first excited state. For most inert atoms, the energy difference between the ground state and the first excited state (about three quarters of the ionization potential; see Table 2) is much larger than the energy difference between higher excited states. Therefore, it is a good approximation to assume that k_1, the rate constant of atoms being excited from the ground state to the first excited state, is much smaller than k_i ($i = 2, 3, \ldots m$), the rate constants for further excitation from level i to level i+1. Furthermore, assuming the effective lifetimes of the intermediate excited states with respect to radiative decay and collisional de-excitation are sufficiently long (as was assumed in the two-step process), the rate equations are:

$$\begin{aligned}
\frac{dn_1}{dt} &= k_1 n_o^2 - k_2 n_o n_1 \\
\frac{dn_2}{dt} &= k_2 n_o n_1 - k_3 n_o n_2 \\
&\cdots\cdots\cdots \\
\frac{dn_m^+}{dt} &= k_m n_{m-1} n_o,
\end{aligned} \tag{22}$$

where $n_o, n_1, \ldots n_m^+$ are the number densities of atoms in the ground state, first excited state, ..., and ionized state respectively. Assuming $n_o >> \sum_{i=1}^{m} n_i$ and initially $n_1 = n_2 = \ldots = n_m^+ = 0$, then

$$n_1(t) = \frac{k_1}{k_2} n_o(1-e^{-k_2 n_o t})$$

$$n_2(t) = k_1 n_o \left[\frac{1}{k_3}(1-e^{-k_3 n_o t}) - \frac{1}{k_3-k_2}(e^{-k_2 n_o t} - e^{-k_3 n_o t})\right]$$

.....

$$n_{m-1}(t) = k_1 n_o \left[\frac{1}{k_m}(1-e^{-k_m n_o t}) - \frac{1}{k_m-k_{m-1}}(e^{-k_m n_o t} - e^{-k_{m-1} n_o t}) + \ldots\right] \quad (23)$$

$$n_m^+(t) = k_1 n_o \left[n_o t - \frac{1}{k_{m-1}}(1-e^{-k_{m-1} n_o t}) + \ldots\right]$$

To see the general behavior for small time, consider $t \ll 1/k_i$. Then,

$$\begin{aligned} n_1(t) &= k_1 n_o^2 t \\ n_2(t) &= \frac{1}{2} k_1 k_2 n_1 n_o^2 t^2 \\ &\cdots\cdots \\ n_{m-1}(t) &= \frac{k_1 k_2 \cdots k_{m-1}}{(m-1)!} n_1 n_o^{m-1} t^{m-1} \\ n_m^+(t) &= \frac{k_1 k_2 \cdots k_m}{m!} n_1 n_o^m t^m \end{aligned} \quad (24)$$

i.e. $n_m^+(t) \sim t^m$.

As t becomes larger than $1/k_i$, the intermediate levels become saturated. Hence

$$\begin{aligned} n_1 &= \frac{k_1}{k_2} n_o \\ n_2 &= \frac{k_1}{k_3} n_o \\ &\cdots\cdots \end{aligned} \quad (25)$$

$$n_{m-1} = \frac{k_1}{k_m} n_o$$

$$n_m^+ = k_1 n_o^2 t \qquad \text{i.e.} \quad n^+ \sim t. \tag{25}$$

Since we are not interested in the details of the reactions, it is easily seen that the general behavior of the process is governed by two characteristic time scales, $\tau_1 = 1/k_1$, and $\tau^* = \text{Max of } 1/k_2, \ldots 1/k_m$. For $t \ll \tau^*$, $n_m^* \sim t^m$. For $\tau_1 \gg t \gg \tau^*$, $n_m^+ \sim t$, i.e.

$$\frac{dn_m^+}{dt} = k_1 n_o^2, \tag{26}$$

which for large time is equivalent to a one-step ionization process with an effective rate constant k_1 and an effective "excitation time" τ^*. Physically, τ^* is the time required for the populations of all intermediate excited states to become saturated. It will be seen (section 5.2.2) that the experimental results exhibit qualitatively both the "excitation time" delay and subsequent linear increase with time that these considerations predict. A characteristic plot of n_m^+ versus time is shown in figure 1. This simplified ionization model will be used later in gas mixtures, and k_1 and τ^* will be determined experimentally.

2.3 Ionization Rates in Gas Mixtures

In the last section it was seen that after a certain characteristic excitation time, a multi-step process can be thought of as a one-step

process, and the rate constant is simply the rate constant of the rate determining step. Using this result, a simplified model for ionization in gas mixtures is studied in the following manner.

For a gas mixture of m components with number densities $n_1, n_2, \ldots, n_m$ the rate equations can be written as

$$\frac{dn_i^+}{dt} = \sum_{j=1}^{m} k_{ij} n_i n_j \qquad i = 1, 2, \ldots, m. \tag{28}$$

The k_{ij} are the effective rate constants, which can be expressed as

$$k_{ij} = A_{ij} \exp(-E_{ij}/(kT)) \tag{29}$$

where A_{ij} = pre-exponential factor and E_{ij} = activation energy.

More specifically, consider a mixture of argon and small amounts of atomic hydrogen. For the initial stage of ionization, the electron density is low enough so that both electron-atom ionization and electron-ion recombination are neglected for argon. However, the electron-ion recombination rate constant for the hydrogen ion (Massey and Burhop 1952) is 10^3 times larger than that for the argon ion, and the recombination of hydrogen ions may not be negligible. The various possible reactions are then

$$
\begin{aligned}
A + A &\xrightarrow{k_A} A + A^+ + e \\
A + H &\xrightarrow{k_{AH}} A^+ + H + e \\
A + H^+ &\xrightarrow{k_{AH^+}} A^+ + H^+ + e \\
A + H^+ &\xrightarrow{k_T} A^+ + H \\
A + H &\underset{k_{RH}}{\overset{k_H}{\rightleftharpoons}} A + H^+ + e
\end{aligned}
\qquad (30)
$$

The rate equations become

$$
\begin{aligned}
\frac{dn_A^+}{dt} &= k_A(T)\, n_A^{\,2} + k_{AH}(T)\, n_A\, (n_{Ho} - n_H^+) \\
&\quad + k_{AH}(T)\, n_H^+\, n_A + k_T(T)\, n_H^+\, n_A
\end{aligned}
\qquad (31)
$$

$$
\begin{aligned}
\frac{dn_H^+}{dt} &= k_H(T)\, n_A\, (n_{Ho} - n_H^+) - k_T(T)\, n_H^+\, n_A \\
&\quad - k_{RH}(T)\, n_H^+\, (n_H^+ + n_A^+)
\end{aligned}
$$

or

$$
\begin{aligned}
\frac{dn_H^+}{dt} &= A - Bn_H^+ - Cn_H^{+2} \\
\frac{dn_A^+}{dt} &= D + En_H^+
\end{aligned}
\qquad (32)
$$

where $A = k_H(T) n_A n_{Ho}$

$B = k_T(T) n_A + k_H(T) n_A$

$C = k_{RH}(T)$

$D = k_A(T) n_A^2 + k_{AH}(T) n_A n_{Ho}$

$E = k_{AH} + (T) n_A + k_T(T) n_A - k_{AH}(T) n_A$

and n_{Ao}, n_{Ho} = initial number density of argon and hydrogen

n_A, n_H = number density of argon and hydrogen

n_A^+, n_H^+ = ion number density of argon and hydrogen.

Assuming $n_A \simeq n_{Ao}$ (because $n_{Ao} \gg n_A^+$) and initially $n_A^+ = n_H^+ = 0$, then

$$n_H^+ = \frac{n_\infty \tanh \frac{t}{\tau_\infty}}{1 - B \frac{\tau_\infty}{2} \left(1 - \tanh \frac{t}{\tau_\infty}\right)}$$

$$n_A^+ = Dt + E \int n_H^+ \, dt \qquad (33)$$

where

$$n_\infty = \frac{2A}{\sqrt{B^2 + 4AC} + B}$$

$$\tau_\infty = \frac{2}{\sqrt{B^2 + 4AC} + B} \qquad (34)$$

A characteristic plot of n_H^+ and n_A^+ versus time is shown in figure 2. n_H^+ becomes saturated at τ_∞ and n_A^+ increases linearly either after $t = \tau_\infty$ or earlier depending on whether the coupling parameter E is larger or smaller than D/n_H^+.

Using this model, the complicated ionization processes in a gas mixture can be simplified. The essential features, such as activation energies, effective collision cross sections etc., of the ionization processes can then be obtained from the experiment.

III. APPARATUS AND PROCEDURE

In this experiment, ionizing gas in the 17-inch shock tube is the source of ions for the spectrometer and an electron beam is not needed to ionize the sample. The spectrometer is mounted on the end wall of the shock tube (figure 3). Ions produced by thermal ionization behind a reflected shock wave are sampled through small orifices in the end wall after they have diffused through the dense thermal layer adjacent to the wall.

In this section a general description of the mass spectrometer, the shock tube and the apparatus is given. Furthermore, the ion diffusion is analyzed in detail to assess the possibility that the sampling process alters the reaction products.

3.1 Mass Spectrometer

The requirements for a mass spectrometer to be used in the study of ionization in a shock tube are a) fast time response, b) high sensitivity, and c) simplicity of structure, rather than a high resolving power. Modern mass spectrometry makes use of alternating-gradient-focusing, double-focusing and cyclotron-resonance etc. A resolving power of one part in 25, 000 can easily be achieved, but for our modest purpose, this is unnecessary. The simple Nier type mass spectrometer (Nier 1947) is well suited to our purposes.

Recently, time-of-flight mass spectrometers have frequently been used in shock tube studies of chemical kinetics at high temperatures (Bradley and Kistiakowsky 1961, Dove and Moulton 1965). This method has the advantage of measuring the entire spectrum

at one or more different times during a run. In comparison, the presently used magnetic mass spectrometer suffers from the disadvantage of requiring several runs to obtain a complete spectrum but has the advantage of measuring the continuous time history of a definite mass. This can be important in understanding the sampling process and the reactions taking place in the hot gas.

The mass spectrometer we have built is a modification of the Nier (1947) type mass spectrometer (Sturtevant 1966). The unique feature of this mass spectrometer is its fast time response (one microsecond rise time), which is necessary for studies of shock-tube flows. This is achieved by using a ten-stage electron multiplier (DuMont SPM 18-01-401) followed by an operational amplifier (Philbrick Type P25AH) to amplify the ion current from the collector.

Because of space requirements for the removable electron-beam ion source, and to eliminate the transmission of shock tube vibration (due to diaphragm bursting) to the mass spectrometer, a bellows and a "cookie cutter" are used as shown in figure 3. The cookie cutter is a 3-inch diameter tube which extends upstream into the shock tube and cuts a piece from the center of the shock wave. A thin metal diaphragm containing the sampling orifices closes the other end of the cookie cutter and forms the real end wall (about 150 mm downstream of the 17-inch shock tube end wall) in these experiments.

A "spectrometer valve", a rectangular block which contains the electron-beam ion source and the false end wall, slides between two fixed plates and can either align the mass spectrometer with the shock tube or the ion source, and separate it from the other. This

spectrometer valve is pneumatically actuated. A few milliseconds after each run the gate signal from an oscilloscope starts the valve closing and turns off the high voltage.

The ion source, which is used to set the mass peak, consists of a filament to emit electrons, an accelerating electrode, and a field magnet (about 150 gauss) to focus the electron beam. The filament is a tungsten ribbon hairpin (0.025 mm x 0.75 mm x 10 mm) mounted between two tungsten leads (0.75 mm diameter wire), which are mounted on glass. The filament current (0 to 6 amperes) is supplied by a 6-volt storage battery. The electrons, which are accelerated to a voltage of from 0 to 90 volts by two 90 volt dry batteries, ionize the neutral atoms in the ion source (figure 3).

Ions which are either produced in the ion source or sampled from the shock tube through an orifice, are drawn out (figure 4), collimated, accelerated to a potential of from -1,000 to - 2,000 volts, analyzed and focused by a 6-inch-radius, 60° sector magnetic field (which can be varied from 100 to 4,000 gauss) and, finally, collected by the first dynode of the electron-multiplier. When the electron-multiplier output is coupled by an operational amplifier to a Tektronix type 555 oscilloscope with a type L plug in preamplifier, the time response is one microsecond and the total current gain is 2,000,000 (1,000 due to the electron-multiplier, 2,000 due to the operational amplifier). If a sampling diaphragm containing six 0.15 mm diameter holes is used, an ion density of 10^{10} cm^{-3} in the shock tube can easily be detected.

The envelope of the mass spectrometer is constructed entirely of metal (stainless steel) and the flanged joints are sealed by neoprene O-rings. The pressure inside is pumped to 10^{-6} mmHg and is maintained at less than 7×10^{-5} mmHg during each run by a 4-inch oil diffusion pump (CEC type MCF-300). This pump is isolated from the spectrometer by a "straight-through" liquid nitrogen cold trap. The pressure is measured continuously by a cold cathode ionization vacuum gauge which is calibrated against a McLeod gauge.

The mass resolving power is adjustable (by changing slit dimensions) from 1 in 10 to 1 in 200, so we can either measure several neighboring mass peaks at a time or measure each mass peak individually. If a 0.75 mm x 15 mm slit is used on the collector, a resolution of 1 in 200 is obtained. The stability of the power supplies for the acceleration voltage and the magnetic coil current is such that when the mass spectrometer is set on a certain mass peak there is no perceptible drift for periods of over half an hour.

3.2 17-inch Shock Tube

In this study the ions which enter the mass spectrometer are produced by thermal ionization behind a reflected shock wave. The shock tube used is the GALCIT 17-inch diameter shock tube (Liepmann, Roshko, Coles and Sturtevant, 1962) which was designed for basic experimental research in gas dynamics. The advantages of this shock tube are its low leak rate which gives relatively high purity test gases, its unique diaphragm-opening mechanism which can precisely reproduce the shock strength time after time, and its test

times which are longer than those in smaller diameter tubes (Roshko 1960). These are the essential requirements for this experiment.

As a vacuum system, the 17-inch shock tube is well designed and vacuum tight. There are two pumping systems, the primary one and the high vacuum one. The primary pumping system consists of two German Heraeus pumps in series. The fore pump, a type E225 (pumping speed 132 cfm, ultimate pressure 20 μHg) and the vacuum pump, a Roots-type blower VPR-1600 (pumping speed 400 liter/sec, ultimate pressure 0.5 μHg) pump the whole driven section from atmospheric pressure to about $\frac{1}{2}$ μHg in 10 minutes. To attain a higher vacuum, the other independent high vacuum system, which consists of a Kinney KC 46 in series with a smaller but 2-stage Heraeus Roots blower, the VPR-152A (pumping speed 40 liter/sec, ultimate pressure 2×10^{-6} mmHg) and a liquid nitrogen trap, pump the tube from $\frac{1}{2}$ μHg to 2×10^{-6} mmHg in $\frac{1}{2}$ hour. After three hours continuous pumping, the degassing rate is about 0.1 μ/hr.

3.3 Heat Gauge

One important shock tube diagnostic tool is the heat gauge (thin film heat transfer gauge), which has been widely used with considerable success. The main interest here is in using the heat gauge to measure the shock speed and to trigger the instruments. It has been noted that at higher shock Mach numbers, the heat gauge is "shorted" by the electrons produced in the ionization process (Jahn and Weimer 1958). This shorting tends to interfere with the signals and produces spurious results. To eliminate the shorting effect a

non-shorting heat gauge circuit was built which makes it possible to measure shock speeds and also to trigger the instruments for Mach numbers up to 12 in xenon. Furthermore, electronic noise due to ground loops in the shock tube and circuits, which has been troublesome in the past, is reduced.

The gauge (Liepmann, Roshko, Coles and Sturtevant 1962) is made of platinum film plated on a 1-inch diameter pyrex plug, and mounted in the instrumentation access hole of the shock tube side wall or end wall. The operation and the circuit of ordinary heat gauges are given elsewhere (Klein 1967).

Based on the observation that when the heat gauge is biased at negative voltage it collects ions and vice versa, the non-shorting circuit simply floats both terminals of the thin film and biases them to a certain negative voltage. The electrons are then repelled by the negative potential and the ions are collected. The voltage difference due to the ions collected by the thin film is approximately the same at both terminals*, so that when the voltage difference (measured by a differential amplifier, figure 5) between these terminals is measured, the ion current cancels out and only the true heat transfer signal is amplified.

Using this non-shorting circuit, the heat transfer signal in a partially ionized gas is distinguishable from the electronic noise, and shock arrival times and velocities are measured up to a shock Mach

---

* To maintain a constant current through the thin film, there is a small voltage difference between the two terminals. Therefore, the ions collected at the two terminals may not be the same.

number of 11.6 in xenon (p_1 = 100 μHg). Typical non-shorting heat gauge traces and ordinary heat gauge traces under the same conditions are shown in figure 6, where the bias voltage is -9 v. The ordinary heat gauge signal is shorted by electrons or ions right after the incident shock or the reflected shock arrives, while the non-shorting heat gauge output still reads correctly as though there were no electron or ion influences. The range of validity of the heat gauge can thus be extended to either higher Mach number or lower pressure shock waves. It is hoped that this non-shorting heat gauge can be further developed to measure heat transfer on the end wall at very high shock Mach numbers without being disturbed by electrons or ions.

3.4 Experimental Procedure

To measure the mass spectrum of the ionizing gas behind the reflected shock wave, only one mass peak is observed during each run. This gives a continuous time history of the ionization process with microsecond resolution, which is unattainable when making a full scan to all mass peaks. Of course, several runs are required to obtain a complete spectrum. This is time consuming because a long pumping time is required to reduce the degassing rate and to maintain a high degree of purity in the shock tube.

Pre-setting the mass peak

For each run, just before bursting the diaphragm, the desired mass peak is set by using the removable electron-beam ion source. Then the source is moved aside, a metal diaphragm end wall containing the sampling orifices taking its place (figure 3).

Impurity level

To minimize the impurity level, the time elapsed between closing the vacuum pump valves and bursting the shock tube diaphragm is kept as short as possible, usually about one minute. Before each run the degassing rate (at 4×10^{-6} mmHg, the pressure is doubled after one minute) in the tube is measured. Also, the tube pressure (about 4×10^{-6} mmHg) is measured just before introducing the test gas, with the spectrometer valve opened. This is done to ensure that no foreign gas is dumped into the tube by closing of the valves. For a typical run, say $p_1 = 180$ μHg, the impurity level is about 50 ppm (calculated from tube pressure and degassing rate).

Instrumentation

The shock velocity is measured near the end of the driven section by two thin film heat transfer gauges (section 3.3). Another thin film heat gauge is mounted on the shock tube end wall (figure 3) to trigger the instruments and to determine the shock arrival time at the end wall. Two tektronix type 555 dual-beam oscilloscopes were used, with one beam recording the end wall trace to give the shock arrival time and assure repeatability. The three other beams were used to record the electron-multiplier output, each beam having a different amplification and sweep speed to give the details in the different regions of interest.

Operating sequence

The operating sequence was as follows: install the suitable diaphragm and knife edges; pump the driven section to 10^{-6} mmHg and the driver section to about 1 μHg; measure the leak rate and determine the impurity level; use the electron-beam ion source and the electron-multiplier output to set the appropriate mass peak; remove the ion source; connect the electron-multiplier output to the operational amplifier (output of this amplifier is connected to oscilloscopes); measure the tube pressure again; close the pump valve; introduce the test gas; introduce the driver gas; reset the counter and oscilloscopes; open the camera shutter; fire.

Data reduction

Since all traces were recorded on polaroid film, the data reduction was relatively easy and direct. The Mach number was measured for each run, and was found to be reproducible to within $\pm$ 0.6 per cent which corresponded to a temperature variation of $\pm$ 7 per cent. The impurity level in the shock tube was controlled by varying the pumping time and monitering the leak rate. A further check on the impurity level was rendered by the trace of the end wall heat gauge, which is sensitive to both the temperature and the degree of ionization.

IV. SAMPLING PROCESS

As in all sampling experiments, the question of whether the reaction products are altered during the sampling operation is of primary importance. Consequently, the sampling process is studied in some detail.

Ideal sampling occurs when all the reactions in the sampled gas are frozen from the time it leaves the active region (between the reflected shock wave and the end-wall thermal layer) until it enters the mass spectrometer and is finally collected by the electron-multiplier collector. This can only be achieved by rapidly expanding the sampled gas to a low temperature and density without any energetic collisions taking place, e.g. by free-molecular effusion from an orifice.

In the actual case there is always a layer of cool and dense gas (thermal layer) adjacent to the end wall. As was discussed by Sturtevant (1966), two somewhat different cases arise depending on whether the orifice diameter d is greater or less than the thermal layer thickness δ. In experiments at relatively high pressure $d \gg \delta$, and the flow into the orifice is inviscid, while at lower pressures $d \ll \delta$, the sampled gas first diffuses through the thermal layer before entering the field of influence of the orifice (section 4.2). In either case, there are certain difficulties in generating a free-molecular beam from a high-pressure jet. It is important to note that

the free-molecular limit $Kn > 1$*, can probably never be realized in shock-tube sampling experiments. A typical test condition (Table 1) shows that the mean free path $\lambda_{wall} = 8 \times 10^{-5}$ cm and the orifice diameter $d = 0.015$ cm. This gives that $Kn = 0(10^{-3})$. In this experiment, before the sampled gas can reach the sampling orifice it has to diffuse through the dense thermal layer. A simplified analysis of this process is given in the following sections.

4.1 Diffusion in the Thermal Layer

As a strong normal shock wave reflects and propagates away from the shock tube end wall, it leaves behind a hot, stagnant body of gas. The gas adjacent to the heat-conducting end wall is cooled by heat transfer and forms an end-wall thermal layer. The gas density and temperature in this growing thermal layer are given by the well-known results of Goldsworthy (1958) for a perfect gas with thermal conductivity proportional to temperature

$$\frac{T}{T_5} = \frac{\rho_5}{\rho} = \left[1 + \left(\frac{T_5}{T_1} - 1\right) \operatorname{erf} \eta\right] \Big/ \frac{T_5}{T_1} \tag{1}$$

where T_1 is the wall and initial gas temperature, T_5 is the frozen gas temperature behind the reflected shock wave and η is a boundary layer coordinate, defined by

$$\eta = \frac{X}{2(K_5 t)^{1/2}}$$
$$X = \int_o^x \frac{\rho}{\rho_5}\, dx \tag{2}$$

---

* Knudsen number $Kn = \lambda^*/d$ where λ^* is the mean free path at the sonic point in the sampling orifice, d is the diameter of the sampling orifice.

K_5 is the thermal diffusivity, t is the time after the shock wave has reached the wall, and x is the distance from the end wall. The induced velocity (velocity induced by accumulation of mass in the end wall thermal layer) is then

$$v = -\left(\frac{K_5}{\pi t}\right)^{1/2}\left(1 - \frac{T_1}{T_5}\right)\left(1 - e^{-\eta^2}\right) \tag{3}$$

The problem encountered here is to find the charged particle density distribution in the thermal layer, where the gas density is so high that the local mean free path is much smaller than the orifice diameter. A continuum description including the effects of viscosity, heat conductivity, diffusion of the many species, and electrical conduction is necessary. Clearly, a general analytic solution to such a complex problem is not obtainable. Fortunately, under the assumption of quasi-neutrality, and a transformation of both dependent variables and independent variables, it is possible to decouple the diffusion of the charged particles from the mass motion of the neutral gas. Then the problem is reduced to a simple diffusion problem.

Assuming that recombination and ionization are negligible in the thermal layer (an estimation of the reactions in the thermal layer will be given in section 4. 3), the ion flux and electron flux are then given by:

$$\underline{\Gamma}^{+} = n^{+}\underline{u}^{+} = - \rho D^{+} \text{ grad } \frac{n^{+}}{\rho} + \mu^{+} \underline{E}\, n^{+}$$

$$\underline{\Gamma}^{-} = n^{-}\underline{u}^{-} = - \rho D^{-} \text{ grad } \frac{n^{-}}{\rho} - \mu^{-} \underline{E}\, n^{-} \qquad (4)$$

where $n^{\pm}$ are ion and electron densities

$u^{\pm}$ are ion and electron diffusion velocities

$D^{\pm}$ are ion and electron diffusion coefficients

$\mu^{\pm}$ are ion and electron mobilities

$\underline{E}$ is the electric field induced by the charged particles.

As pointed out by Su (1965), quasi-neutrality is a good approximation for ion and electron diffusion in the thermal layer down to the edge of the sheath layer, which is about a few Debye lengths from the end wall. This ambipolar diffusion assumption greatly simplifies the problem. The ion flux then becomes:

$$\underline{\Gamma} = n\underline{u} = - \rho D \left[\text{grad } \frac{n}{\rho} \right] \qquad (5)$$

where n is the ion density

$\underline{u}$ is the ion diffusion velocity

D is the ambipolar diffusion coefficient,

$$D = \frac{D^{+}\mu^{-} + D^{-}\mu^{+}}{\mu^{+} + \mu^{-}} \simeq 2\, D^{+}$$

Assuming the diffusion coefficient to be proportional to T/ρ, then

$$D = Le\, K_5 \frac{T}{T_5} \frac{\rho_5}{\rho} \tag{6}$$

where the Lewis number Le is taken to be constant. For slightly ionized gas at a constant pressure, the charged-particle continuity equation is (Hirschfelder, Curtiss and Bird 1954)

$$n_t + [n\,(u + v)]_x = 0 \tag{7}$$

where v and u are defined in equations (3) and (5) respectively. The continuity equation for a neutral gas is

$$\rho_t + (\rho\, v)_x = 0 \tag{8}$$

Introducing a new dependent variable, the mass fraction,

$$C = m\, n/\rho \tag{9}$$

and a transformation of the independent variables, the Stewartson Transformation,

$$X = \int_0^x \frac{\rho}{\rho_5}\, dx \tag{10}$$

$$\tau = t \tag{11}$$

one arrives at the simple equation

$$C_\tau = D_5 C_{XX} \tag{12}$$

which can easily be solved for various initial and boundary conditions.

a) Condition at infinity

As shown in section 2.2 the rate of ion production is a strong function of temperature, i.e. it is proportional to $\exp(-E_a/kT)$. In the present case, a 5 per cent decrease in temperature cuts the ion production rate in half. Hence it is a good approximation to assume a certain critical temperature, below which the ion production is cut off and above which the reaction remains the same.

The isothermal line $X = X(t;T)$ in the thermal layer is easily found to be

$$X(t;T) = 2(K_5 t)^{1/2} \operatorname{erf}^{-1}\left(\frac{T/T_1 - 1}{T_5/T_1 - 1}\right) \tag{13}$$

Assuming that the reaction is cut off at $T = T_c$, the cut-off line is

$$\delta(t) = 2(K_5 t)^{1/2} \eta_\delta \tag{14}$$

where $$\eta_\delta = \operatorname{erf}^{-1}\left[\frac{T_c/T_1 - 1}{T_5/T_1 - 1}\right] \tag{15}$$

Outside the cut-off line the ion production is assumed to start after a certain excitation time τ^* and increase linearly with time.

b) Initial condition

Initially $n^+ = n^- = 0$ over all space.

c) Condition at wall

The wall is assumed to be perfectly absorbing for all time, i.e. $n = 0$.

The diffusion equation can then be written as

$$C_\tau - D_5 C_{XX} = 0 \tag{12}$$

with a) $C(X \geq 2 (K_5 \tau)^{1/2} \eta_\delta , \tau \geq \tau^*) = \dot{C}_5(\tau - \tau^*)$

b) $C(X < 2 (K_5 \tau^*)^{1/2} \eta_\delta , \tau = \tau^*) = 0$ (16)

c) $C(0, \tau) = 0$

The solution is:

$$C(X, \tau) = \int_0^\infty \int_0^\infty \frac{H(t - \tau^*)\, H\left(\frac{\xi}{2(K_5 t)^{1/2}} - \eta_\delta\right) \dot{C}_5}{(4\pi D_5(\tau - t))^{1/2}} \tag{17}$$

$$\left[\exp\left(-\frac{(X-\xi)^2}{4D_5(\tau - t)}\right) - \exp\left(-\frac{(X+\xi)^2}{4D_5(\tau - t)}\right)\right] d\xi\, dt$$

where H is the Heaviside unit function. This can be further simplified by letting

$$\eta^* = \frac{X}{2(K_5 \tau^*)^{1/2}} \tag{18}$$

Then,

$$\frac{n(\eta^*, \tau - \tau^*)}{\dot{n}_5(\tau - \tau^*)} = \frac{T_{51} \int_0^{\tau - \tau^*} \left[\operatorname{erf} \frac{\eta_\delta \left(\frac{\tau - t}{\tau^*} \right)^{1/2} + \eta^*}{(\mathrm{Le}\, t/\tau^*)^{1/2}} - \operatorname{erf} \frac{\eta_\delta \left(\frac{\tau - t}{\tau^*} \right)^{1/2} - \eta^*}{(\mathrm{Le}\, t/\tau^*)^{1/2}} \right] dt}{2(\tau - \tau^*) \left[1 + (T_{51} - 1) \operatorname{erf} \frac{\eta^*}{(\tau/\tau^*)^{1/2}} \right]} \qquad (19)$$

Numerical results were obtained on the IBM 7094 Computer at the Caltech Computing Center. A typical plot of $n(\eta^*, \tau - \tau^*)$ versus η^* with $\eta_\delta = 1$ and for different times and Le is shown in figures 7 and 8.

Two important parameters, Le and η_δ, are involved in the solution, the former associated with the time scale and the latter with the length scale. The qualitative behavior of the ion density for small η^*, i.e.

$$\eta^* \ll \frac{\left(\frac{\tau}{\tau^*} \right)^{1/2}}{T_{51}} \ll \eta_\delta$$

is that $n/(\dot{n}_5(\tau - \tau^*))$ starts out linearly with η^*. As η^* increases and reaches $0((\tau/\tau^*)^{1/2}/T_{51})$, $n/(\dot{n}_5(\tau - \tau^*))$ flattens out*, seemingly reaching a plateau. As η^* further increases, $n/(\dot{n}_5(\tau - \tau^*))$ increases exponentially with η^* as the edge of the thermal boundary is approached and it reaches a peak just outside the thermal layer.

* This boundary-layer-within-a-boundary-layer-behavior is due to the fact that ions not only diffuse, but are also convected by the neutral gas toward the wall.

4.2 Free Jet Expansion

The ions, after diffusing through the thermal layer, are sampled through small orifices connecting the shock tube to the mass spectrometer. As mentioned before, due to the end wall thermal layer it is impossible for the free molecular flow requirement, $Kn > 1$, to be satisfied. Therefore, a supersonic free jet is formed. The upstream influences of the jet on ion diffusion in the thermal layer and the down stream interaction of the jet with the accelerating slits (figure 4) will be discussed.

Upstream

By continuity, the upstream velocity induced by the jet is proportional to the inverse of the number density and the inverse of the distance squared. Hence, far from the orifice, the flow field and the ion density are not disturbed. At a distance of several diameters from the orifice, however, the jet induced velocity v_J becomes larger than the ion flux velocity u. In the charged particle continuity equation, u and v are then negligible compared to v_J. Thus, for this case equation (7) becomes

$$n_t + [nv_J]_x = 0 \tag{20}$$

Along the center line of the orifice v_J is approximately c/x^2 where c is a constant. Assuming $v_J = c/x^2$ for the whole section, then

$$n_t + \frac{c}{x^2} n_x - \frac{2c}{x^3} n = 0$$

Solving this partial differential equation:

$$n_J(x, t) = x^2 f(t - \frac{x^3}{3c}) \qquad (21)$$

where f is an arbitrary function to be determined by the boundary condition. Matching this solution to the solution of ion density far from the orifice at the position where $u/v_J = 1$, the function f can be uniquely determined.

Downstream

The down stream interaction of the jet with the electrodes is extremely complicated and almost impossible to analyze. Fortunately, in a strong electric field (about 1000 v/cm) the ion velocity is much larger than the jet velocity. Hence, the motion of the ions is approximately decoupled* from the jet. Due to the strong attractive field and the geometry, most of the ions are collected by the drawout-electrode (figure 4); only 0.01 per cent (section 5.1) of the ions pass through the slits and are collected by the electron-multiplier. The present arrangement is good for ion densities of from 10^9 ions/cm^3 to 10^{12} ions/cm^3. Below 10^9 ions/cm^3, the signal to noise ratio of the electron-multiplier output will be less than one. This can be improved by rearranging the accelerating slits or by using a higher gain electron-multiplier. The upper limit is due to the fact that both the effect of the electrostatic sheath in front of the drawout-electrode and the effect of the mutual repulsion of the ions in the jet become important. All

* As will be discussed later, if the ion density becomes too high this decoupling becomes impossible.

these change the efficiency of the electrodes, with the result that makes the sampling a non-linear function of ion density.

Result

In summary, the above results demonstrate that for moderate ion densities, the mass spectrometer output is approximately proportional to n_J, which is computed numerically and plotted against time, together with a measured argon ion trace superimposed for comparison in figure 9. The agreement with the actual mass spectrometer output of argon ions further demonstrates that the sampling technique can be used for accurate measurements of the ionization processes.

4.3 Reactions in the Thermal Layer

It was assumed in the previous section that reactions in the thermal layer are frozen or are negligibly small. To justify this assumption, charge transfer and recombination processes in the thermal layer are studied below.

4.3.1 Charge transfer

In general, the charge transfer process can be written as

$$A^+ + B \xrightarrow{k_{CT}} A + B^+ \tag{22}$$

where A or B^+ may be in an excited state. The rate equation then is

$$\frac{dn_A^+}{dt} = - k_{CT} n_A^+ n_B \tag{23}$$

where k_{CT} is the rate constant for the charge transfer reaction, n_A^+ is the number density of the "A" ions, and n_B is the number density of the "B" atoms. Because the thermal layer is non-steady and non-uniform, the rate constant and the atom number density are functions of time and position. As before if it is assumed that the reaction rate is small compared to the diffusion rate, the reaction can be decoupled from the charge diffusion. Then the ratio of n_A^+, the number of ions left after undergoing charge transfer during the passage and through the thermal layer, and n_A^+, the number of ions entering the thermal layer, is

$$\frac{n_A^+}{n_{A\infty}^+} = \exp\left(-\int_{path} k_{CT}\, n_B\, dt\right) \tag{24}$$

where the integration is performed along the average particle path

$$\frac{dx}{dt} = u + v \tag{25}$$

u and v are defined in equations 8 and 3. The averaged charge transfer rate constant, k_{CT} is defined by

$$\overline{k_{CT}} = \frac{\int_{path} k_{CT}\, n_B\, dt}{n_{B\infty}\, \tau} \tag{26}$$

where $n_{B\infty}$ is the number density of "B" atoms outside the thermal layer and τ is the time after the shock wave is reflected from end

wall. Using n_B and the average particle path calculated from the previous section, i.e.

$$n_B = n_{B\infty} \frac{T_{51}}{1 + (T_{51} - 1)\, \mathrm{erf} \dfrac{\eta^*}{(\tau/\tau^*)^{1/2}}} \tag{27}$$

$$\frac{d\eta^*}{d\,\tau/\tau^*} = - \frac{Le}{4} \frac{C_\eta^*}{C}$$

where C, η^* and τ/τ^* are the mass fraction, dimensionless length variable, and dimensionless time variable as were defined in equations 10 and 18, then $\overline{k_{CT}}$ can be obtained from a numerical integration along the average particle path. The result, as might have been expected, shows that $\overline{k_{CT}}$ is of the order of k_{CT} (outside the thermal layer). A typical value for $\overline{k_{CT}}$, at $T_{51} = 40$, $Le = .25$, $\tau = 100\ \mu sec$ and k_{CT} = constant is $3\, k_{CT}$. Therefore,

$$\frac{n_A^+}{n_{A\infty}^+} \simeq \exp\left(- k_{CT}\, n_{B\infty}\, \tau\right) \tag{28}$$

To find this ratio, an estimate of k_{CT} for various charge transfer processes are given in the following paragraphs.

Symmetrical resonant charge transfer

Symmetrical resonant charge transfer is defined as the charge transfer between like systems. The collision cross section can be calculated from Firsov's theory (Hasted 1962), and usually is very

large. For instance, the charge transfer cross section between argon ions and argon atoms is $6.5 \times 10^{-15} cm^2$ and between xenon ions and xenon atoms is $9.7 \times 10^{-15} cm^2$, i.e. larger than the gas kinetic collision cross sections. It is noted that although this charge transfer process does not result in a loss of ions if they are diffusing through a neutral gas of the same species (i.e. there is no chemical change) it nevertheless does result in a very small diffusion coefficient.

Asymmetric resonant charge transfer

Asymmetric resonant charge transfer (Bates 1962) is defined as charge transfer for which the system that loses the electron is not the same species as the system which gains the electron, but nevertheless the energy balance is very close. The charge transfer cross section between hydrogen ions and oxygen atoms or oxygen ions and hydrogen atoms, that is

$$O(^3p_J) + H^+ \rightleftharpoons H(1S) + O^+(^4S) \qquad \begin{cases} +.01 \text{ ev } (J = 0) \\ +.00 \text{ ev } (J = 1) \\ -.02 \text{ ev } (J = 2) \end{cases} \qquad (29)$$

is maximum (comparable with gas kinetic collision cross section) when the adiabatic parameter $vh/(a\Delta E)$ equals unity, a is a length of the order of 7×10^{-8} cm, ΔE is the energy defect, v is the relative velocity, and h is Planck's constant. In the range of this experiment, the adiabatic parameter is close to one. This raises the possibility of large charge transfer rates between O^+ and H or H^+ and O in the hot gas (experimental results concerning this coupling will be discussed in section 5.2.4). In the thermal layer, where the temper-

ature and the relative velocities are low (section 2.1, equation 7) the adiabatic parameter is considerably less than unity. Reactions in this region and those for which ΔE is large will be discussed below.

Adiabatic region

Except for the symmetric and asymmetric resonant cases, charge transfer cross sections are relatively unknown. They depend on the interaction potential, transmission coefficient, polarizability, etc. However, a qualitative estimation of the cross section is given by Hasted (1962) and Massey and Burhop (1952). In the adiabatic region, i.e. $vh/(a\ \Delta E) \ll 1$, the charge transfer cross section will be small compared with the gas kinetic cross section and in general can be expressed as

$$C\exp\left(-\frac{a\ \Delta E}{4hv}\right) \tag{30}$$

where C is a constant depending on the particular reaction. This exponential form is due to the character of the collision, the ions approaching the atoms with a velocity very small compared with that of the atomic electrons. The latter have therefore plenty of time to readjust themselves to the slowly changing conditions without a transition taking place.

In the range of this experiment, if the energy defect ΔE is 1 ev, the adiabatic parameter is about 0.01. This gives a very small charge transfer cross section. However, for a 'worst case' analysis, the maximum possible charge transfer cross section between A^+ and

H (or other impurities) is the elastic collision cross section due to the polarizability of the atom (Massey and Burhop 1952). This gives a rate constant

$$k_{CT} = \left(\frac{\pi \alpha_p e^2}{\epsilon_o \mu} \right)^{1/2} = 6 \times 10^{-10} \text{cm}^3/\text{sec}$$

where α_p is the polarizability of the atom (assumed to be $2\ A^3$), e is the electronic charge, ϵ_o is the vacuum permittivity, and μ is the reduced mass. For a typical test condition; i.e. argon number density $n_A = 6 \times 10^{16} \text{cm}^{-3}$, impurity level 50 ppm i.e. $n_{I\infty} = 3 \times 10^{12} \text{cm}^{-3}$, $\tau = 100$ sec, then $k_{CT} n_{I\infty} \tau = 0(10^{-1})$. It is believed, therefore, that charge transfer reactions are negligible, except in some experiments where large amounts (0.1 per cent to 2 per cent) of H_2 or O_2 are added.

4.3.2 Recombination

The important recombination reaction in the thermal layer is three body recombination, that is

$$e + A^+ + X \xrightarrow{k_R} A + X \qquad (31)$$

(The reaction $e + e + A^+ \longrightarrow e + A$ occurs relatively infrequently in the present experiment). The rate equation is

$$\frac{dn_A^+}{dt} = - k_R n_A^+ n_e \qquad (32)$$

where n_e is the number density of electrons and is usually equal to n_A^+. More precisely, $n_e = n_A^+ + n_I^+$. Similar to charge transfer (section 4.3.1), the effective rate constant $\bar{k}_R$ is defined by:

$$\bar{k}_R = \frac{\int_{path} k_R \, n_A^+ \, dt}{n_{A\infty}^+ \, \tau} \tag{33}$$

where $n_{A\infty}^+$ is the number density of argon ion outside the thermal layer. $\bar{k}_R$ is of the same order of magnitude as k_R.

For a typical test condition in argon, $k_R = 6.8 \times 10^{-11} cm^3/sec$ (Massey and Burhop 1952), $n_{A\infty}^+ \simeq 10^{12} cm^{-3}$ and at $\tau = 100 \mu sec$, $k_R n_{A\infty}^+ \tau = 0(10^{-2})$. Hence, the recombination rate is negligible compared to the diffusion rate in these experiments. On the basis of the above results it can be concluded that in these experiments the reactions in the thermal layer have negligible effect on the diffusion process provided that the amount of impurity is not too high (less than 50 ppm).

V. RESULTS AND DISCUSSION

5.1 Calibration of Mass Spectrometer

An important, and also difficult part of the study is the calibration. The ions formed in the hot gas must diffuse through the end wall thermal layer, expand through the orifice, be accelerated and collimated by the various electrodes, and then finally focused and analyzed by the magnetic field before being collected by the electron-multiplier collector, as is discussed in IV. An overall calibration constant of the mass spectrometer is defined as the ratio of the measured electron-multiplier output current to the ion number density in the hot gas. Due to the non-steady nature of the end wall thermal layer, the mass spectrometer has to be calibrated dynamically, which seems to be an impossible task.

Hydrogen calibration

Fortunately, in "pure" argon (defined in 5.2) with 0.1 per cent or 0.5 per cent H_2 mixed in argon, the measured ion traces of hydrogen reach equilibrium before the test time is ended (as will be shown in the next section). In these cases an approximate calibration constant for the 1 amu peak at 14, 300^{o}K, can be obtained, if it is assumed that the hydrogen atoms are nearly fully ionized (Appendix A). The result is 6×10^{-23} amp/ions/cm^3. This is obtained from the results of the highest temperature (14, 300^{o}K) and lowest impurity level (50 ppm) runs in these experiments (an averaged value of the calibration constant over three different temperatures is 4×10^{-23} amp/ions/cm^3).

This calibration constant agrees in same order of magnitude with the calculated value, which takes account of the thermal layer diffusion (the ratio of ion density in the shock heated gas to that at the orifice is 0.1), the jet (the jet flux, 3×10^{-18} amp/ions/cm^3, coming out from the sampling orifice is obtained by assuming isentropic nozzle flow), and the efficiency of the accelerating slits (2.5×10^{-4}, which is obtained by measuring the ratio of ions collected by the collector to that collected by the accelerating slits). Using this calibration constant the absolute values of the ionization collision cross section of hydrogen can be obtained.

Other calibration

For argon or xenon, an approximate calibration can be made by using Kelly's (1966) rate constant for argon ionization to calculate the ion density in the hot gas. The calibration constant thus obtained is an order of magnitude less than the hydrogen calibration constant. The reason for this difference is not clear. It may be either that the calibration constant depends on the mass or that the rate constant obtained by Kelly is too high (more comparison with Kelly's results will be given later). Nevertheless, to obtain the relative ionization rates, the activation potentials, etc. the calibration constant is not necessary.

5.2 Shock Heated Argon

Test conditions

The test conditions (Table 1 and Appendix A) in this experiment are chosen such that the test time is long, the interaction in the

thermal boundary layer is low and the ion density is high enough to be measured. The conditions behind a reflected shock wave are calculated for Mach numbers from 6.8 to 8.0 which correspond to frozen temperatures behind the reflected shock wave, T_5, from 10,000°K to 14,300°K, pressures, p_5, from 18 mmHg to 80 mmHg and densities, n_5, from 5.8×10^{16} to 6×10^{16} cm^{-3} respectively. The test time of about 400 microseconds is governed by the length of the "cookie cutter" as shown in figure 10. The ionization relaxation time is about 2,000 microseconds (extrapolated from Petschek and Byron, 1957). The equilibrium ionization levels are about 1.5 per cent to 5.5 per cent, corresponding to equilibrium temperatures from 8,600°K to 9,400°K.

Impurities

As was discussed in section 3.4 the impurity level for each run is calculated from the degassing rate and the time elapsed between closing the pump valve and bursting the shock tube diaphragm. For average "pure" runs, the impurity level is about 50 ppm (p_1 = 180 μHg) where, in general, the dominate components of the impurities are measured with a residual gas analyzer to be: H_2O, N_2, H_2, O, H, N, O_2, etc. (order in decreasing abundance). Therefore, in this experiment "pure argon" means the impurity level is 50 ppm, "0.1 per cent H_2 in argon" means the impurity level is the same, 50 ppm, but with 0.1 per cent H_2 added, and similarly for "0.5 per cent H_2 in argon" and "0.5 per cent O_2 in argon" etc.

5.2.1 Ionic products in "pure" argon

The various ionic products produced in the initial stage of ionization in pure argon have been measured with the mass spectrometer. A surprisingly large number of different ions was observed (Sturtevant 1966) with hydrogen ions and oxygen ions predominating, each being an order of magnitude more abundant than argon ions. The major source of O^+ and H^+ is probably water vapor, the most abundant component of the impurities. Other mass peaks that have been observed in about the same quantity as argon ions are 41(AH^+), 23(Na^+), 12(C^+), 14(N^+), 32(O_2^+), and 39amu(K^+). It is noted that the relative amount of these impurity ions are not repeatable for different series of runs (Table 3), which are separated by a long time (about one year) and which used different ways of pumping*. This might be due to the change of the relative abundance in the impurities for different series of runs. Also a small amount of ionization products with masses of 17(OH^+), 18(H_2O^+), 20(A^{++}), and 28amu(N_2^+), but no discernible amounts of 2(H_2^+) and 80amu(A_2^+) have been observed. These suggest that hydrogen and oxygen are the main contributers to the observed impurity effect. The next step is to study why the ionization of O and H is so efficient and how it affects the ionization of argon.

---

* In the later runs, pure nitrogen was used instead of room air to fill the shock tube to atmospheric pressure for diaphragm changing, in order to eliminate the source of water vapor absorbed on the shock tube wall and later degassed as an impurity.

5.2.2 Character of the ion traces

A series of experiments were conducted in "pure" argon, 0.1 per cent H_2 in argon, 0.5 per cent H_2 in argon, and 0.5 per cent O_2 in argon. The continuous history of ion products of mass 40, 16 and 1 amu was recorded. Typical superimposed traces are shown in figure 11.

Argon

The ion current of argon (figure 9), after a certain excitation time (about 30 microseconds), starts increasing linearly with time until the end of the test time (about 400 microseconds). This behavior is consistent with that predicted by the discussion in section 2.2.

Hydrogen

The hydrogen ion trace is of quite a different nature than the argon ion trace. The hydrogen atom also seems to start ionizing linearly with time, but reaches equilibrium before the test time ends. This can be understood by looking at the Saha equation for gas mixtures (Appendix A) and the rate equations (section 2.3 and figure 2). The rate of ionization for the hydrogen atom is fast and quasi-equilibrium or steady state is reached, that is, the hydrogen is in equilibrium with the argon which is still at the frozen temperature and ionizing slowly. As time goes on, more argon atoms are ionized, the gas temperature decreases, the degree of ionization of hydrogen decreases and it eventually reaches a lower true equilibrium.

Oxygen

The ion traces of oxygen behave more or less like hydrogen, but at the end of the test time the ion current is still approaching the equilibrium level.

Result

Within the limit of experimental accuracy, the character of the traces indicates that the initial stage of ionization does agree with the multi-step ionization model, (where radiative decay and the collisional de-excitation are sufficiently slow compared to the ionization rate) and the theoretical calculation of ionization in a gas mixture.

5.2.3 Rate constants and Arrhenius plots

For times larger than a certain characteristic time ($t > \tau^*$) as discussed in section 2.2 the multi-step ionization process is equivalent to one-step ionization process with an effective rate constant k^*, which can be expressed as $S(kT)^{1/2} + n(1 + \frac{n!}{(n+1)!} \frac{E^*}{kT})e^{-E^*/kT}$ (equation 2-15). Thus it is possible to find E^* by an Arrhenius plot. That is, the semi-logarithmic plot of $\frac{dn^+}{dt}$ versus $1/(kT)$ should be a straight line whose slope determines E^*.

Argon

The rate of increase of the ions was measured from the oscillograms and plotted against the inverse of the temperature. Assuming that $n = 1$ as suggested by Kelly (1966), then the least square fit of the Arrhenius plot for pure argon (figure 13) yields an

effective activation energy for ionizing an argon atom, $E_A = 12.4 \pm 0.7$ ev, which agrees within the experimental scatter with the value (11.9 ev) found by Kelly (1966).

This agreement is significant in that Kelly's experiments were conducted in high purity argon (impurity level of about 1 ppm), as compared with our lower purity shock tube. This shows that a mass spectrometer, which discriminates between individual species in the ionizing gas, measuring the argon ion density instead of the total charge density, has an important advantage over other methods. That is, if the argon ionization is not strongly coupled with impurity ionization (a much weaker requirement than that the impurity ionization does not contribute to the charge density) then the pure gas ionization rates can be measured in rather more impure gases than otherwise possible.

To go one step further, using the calibration constant of the mass spectrometer (assuming the same constant as for the 1 amu peak) the absolute value of the ionization cross section S_{AA} can then be determined from the measured ion current and activation energy. This gives $S_{AA} = 0(10^{-20})$ cm^2, which is an order of magnitude less than Kelly's value. This point discussed from a different point of view in section 5.1.

Hydrogen

An Arrhenius plot (figure 14) for the hydrogen ions in pure argon gives an effective activation energy for ionizing a hydrogen atom $E_H = 9.8 \pm 1.1$ ev (assuming $n = 0$). As with argon, this value

agrees, within experimental accuracy, with the energy of the first excited state (2S) of H (10.3 ev). As shown in Appendix B, the H(2S) state is a metastable state which has a very long average lifetime. Hence if it is assumed that the 2S state can be collisionally populated, then it follows that the ionization of hydrogen atoms can take place via a multi-step process.

The simplified theoretical model of ionization in a gas mixture cannot possibly do more to describe this complex process than to give a crude demonstration of the enormous observed rate of hydrogen ionization. The relative magnitude of the effective cross section S_{HA} (section 2.1, equation 12) can be determined by ratioing $\left(\frac{dn_A^+}{dt}\right)_{\text{pure A}}$ and $\left(\frac{dn_H^+}{dt}\right)_{0.5 \text{ per cent } H_2 \text{ in A}'}$ using the experimentally measured activation energies. This gives $S_{HA}/S_{AA} = 0(10^3)$. It is noted that this ratio is nominally independent of the mass spectrometer calibration and other instrumental factors, except for the mass dependence (section 5.1).

The absolute value of the effective cross section S_{HA} can be obtained by using the calibration constant of the mass spectrometer, the measured activation energy and the measured hydrogen ion current in pure argon. The result is $S_{HA} = 0(10^{-17})\text{cm}^2$, which is comparable with the gas kinetic elastic collision cross section. This striking result explains why hydrogen atoms are ionized so efficiently, even though their effective activation energy is relatively high.

5.2.4 Effects of addition of hydrogen to "pure" argon

In the argon runs with 0.1 per cent and 0.5 per cent H_2 added, the measured ionization products of atomic argon and hydrogen both increases; argon a few times (figure 15) and hydrogen hundreds of times (figure 16). No ionization products of hydrogen molecules were observed. The increase of argon ion current is most probably due to the charge transfer between hydrogen ions and argon atoms, and the ionization of argon atoms by collisions with hydrogen atoms.

The increase of hydrogen ion current shows that hydrogen atoms are easily ionized in the gas phase eliminating the need to a complicated surface process (Creswell, Di Valentin and Dove 1966). A further support of this point is rendered by putting 0.5 per cent D_2 in argon. This gives the same results as 0.5 per cent H_2 in argon with D^+ ions observed instead of H^+ ions.

The decrease of oxygen ion current upon addition of H_2 (figure 17), indicates that charge transfer from H^+ to O is small as expected (section 4.3.1).

5.2.5 Effects of addition of oxygen to "pure" argon

To observe the effect of adding oxygen to argon, a few runs with 0.5 per cent O_2 in argon were performed. The results showed that the amount of argon ions and oxygen ions were about the same, but that the hydrogen ion current decreased by almost an order of magnitude from the "pure" argon runs. This certainly implies that the possibility of charge transfer from O^+ to H is small.

The amount of oxygen molecular ion current increased twenty times as compared to the pure argon runs. The reason for the increase of O_2^+ may either be that some oxygen molecules become ionized before being dissociated, or that oxygen molecules are not completely dissociated in the cold end wall thermal layer, and become ionized by charge transfer with hydrogen ions.

5.2.6 Effects of addition of xenon to "pure" argon

To find the effects of a small amount of xenon in argon, 0.5 per cent Xe was added. A typical ion trace of xenon is shown in figure 18. It increases linearly with time and never becomes saturated before the end of the test time, in contrast with hydrogen ion traces. It might be argued from the rate equations (section 2.3) and the Saha equations (Appendix A) that the lack of saturation in the xenon traces is due to a low activation energy and the saturation of the hydrogen trace is due to a high pre-exponential factor (as, in fact, it is).

The Arrhenius plot of the xenon ion current gives an activation energy of 9 ev. The effective cross section (obtained by using the calibration constant for the 1 amu peak) of ionizing xenon in argon S_{XeA} is of the order of $10^{-19} cm^2$, which is an order of magnitude larger than the value obtained by Kelly (1966), who assumed that $S_{XeXe} = S_{XeA}$, and $S_{AA} = S_{AXe}$. The reason for the difference is that the microwave probe used by Kelly can only measure electron density. Contributions to the electron density may be from either argon or xenon ionization. The mass spectrometer, however, can resolve

different ions, and it measures each ion density separately. This is an advantage of using a mass spectrometer to study ionization in gas mixtures.

It is noted that the measured argon ion current decreases four times when 0.5 per cent Xe is added. Since charge transfer between argon ions and xenon atoms is very small (because the amount of both argon ions and xenon atoms are small), it is suggested that Penning ionization (ionization of xenon atoms by excited argon atoms, Massey and Burhop 1952), might be important. This would explain why the effective cross section S_{XeA} is an order of magnitude larger than the effective cross section S_{XeXe} (section 5.3).

5.3 Shock Heated Xenon

Test Conditions

A limited number of runs in pure xenon have been performed. The Mach number ranged from 8 to 11.6, which corresponded to frozen temperatures, T_5, from 14,000°K to 30,000°K, and pressures, p_5, from 45 mmHg to 98 mmHg respectively (Table 1 and Appendix A).

Character of the Ion Traces

The character of the ion trace initially resembled the 40 amu ion trace in "pure" argon. After a certain time, however, the ion density seemed to reach a plateau, after which it increased rapidly (figure 18). The ion density around the plateau region is far from the equilibrium ion density; only about 1 per cent of the equilibrium value. It is believed that this is due to the formation of a sheath in front of the drawout electrode and the effect of charge repulsion in the ion beam in

the mass spectrometer (section 4.2). As discussed in section 4.2, the sampling process is not fully understood for ion densities larger than $10^{12} cm^{-3}$, but some information can still be obtained in the early part of the run when the ion density is less than $10^{12} cm^{-3}$.

Arrhenius Plot

The rate of increase of the ions was measured from the oscillogram, and plotted against the inverse of the temperatures. The plot is shown in figure 19 and a theoretical line using an activation energy $E_{Xe} = 8.3$ ev and a cross section $S_{XeXe} = 10^{-20} cm^2$ is drawn through the experimental points for which it is believed $n^+ < 10^{12} cm^{-3}$. The measured points fit the theoretical line very well, except for those high temperature runs, where the observed ion densities were much higher than expected. A simple calculation easily demonstrates that this higher ionization rate can be due to the contribution of electron-atom ionization.

Result

The result indicates that the initial ionization of xenon is due to atom-atom ionization with an activation energy $E_{Xe} = 8.3$ ev and an effective cross section $S_{XeXe} = 10^{-20} cm^2$. The values are consistent with those found by Kelly (1966).

VI. CONCLUSION

The main difficulty encountered in using a mass spectrometer for studies of ionization involves the sampling process. In the present arrangement, the ions sampled must diffuse through an end-wall thermal layer before they reach the sampling orifice. A theoretical calculation of this process, with some basic assumptions, agrees with the experimental results, demonstrating that the mass spectrometric technique is capable of giving quantitative results.

The merit of the mass spectrometric study of ionization is that, instead of total charge density, the ionization product of each individual component of a gas mixture can be studied. In the present experiments, this advantage allowed the measurement of pure gas ionization rates in rather impure gases.

To interpret the experimental results, a multi-step ionization model was proposed. The character of the ion traces thus obtained agrees with the experimental results, indicating that the initial ionization does proceed via a multi-step ionization process.

An "impure" gas is a gas mixture; using the mass spectrometer, it has been determined that the dominant impurity ions, formed in argon containing "naturally occuring" impurities, are hydrogen ions and oxygen ions. Further study showed that the activation energy for ionizing H is about 10 ev and the effective ionization cross section is about 10^3 times larger than the corresponding argon ionization cross section. This explains why small amounts of hydrogen, the dominant impurity, strongly affect the rate of ionization of argon.

The experimentally obtained activation energy for argon ionization is 12.4 ± 0.7 ev which agrees within experimental accuracy with Kelly's (1966) results (11.9 ev). Furthermore, the effective ionization cross section for argon ionizing argon, argon ionizing xenon and xenon ionizing xenon are $0(10^{-20})$, $0(10^{-19})$ and $0(10^{-20})$ cm^2 respectively.

APPENDIX A

CALCULATION OF FROZEN AND EQUILIBRIUM CONDITIONS BEHIND REFLECTED SHOCK WAVES

Frozen Conditions

The frozen temperature, pressure and density behind a reflected shock wave can be calculated in two steps, first calculating the conditions behind the incident shock wave and then calculating the conditions behind the reflected shock wave. The normal shock wave jump conditions are as follows (Liepmann and Roshko 1957):

$$\frac{T_2}{T_1} = \frac{[2\gamma M_s^2 - (\gamma-1)][(\gamma-1) M_s^2 + 2]}{(\gamma+1)^2 M_s^2}$$

$$\frac{p_2}{p_1} = \frac{2\gamma M_s^2 - (\gamma-1)}{\gamma + 1}$$

$$\frac{\rho_2}{\rho_1} = \frac{(\gamma+1) M_s^2}{(\gamma-1)M_s^2 + 2}$$

where the subscript 1 denotes conditions just upstream of the shock wave and subscript 2 denotes conditions just downstream of the shock wave. Here γ equals 5/3 (monatonic gases). T_1, p_1, ρ_1 and M_s are all known quantities, hence T_2, p_2, and ρ_2 can be calculated.

For a reflected shock wave, the Mach number is given by

$$M_R = \frac{C_R + U_2}{a_2}$$

$$= \frac{\frac{\rho_2}{\rho_1}\left(\frac{T_2}{T_1}\right)^{1/2}}{M_s}$$

C_R is the reflected shock speed. Similarly,

$$\frac{T_5}{T_2} = \frac{[2\gamma M_R^2 - (\gamma-1)][(\gamma-1) M_R^2 + 2]}{(\gamma+1)^2 M_R^2}$$

$$\frac{p_5}{p_2} = \frac{2\gamma M_R^2 - (\gamma-1)}{\gamma + 1}$$

$$\frac{\rho_5}{\rho_2} = \frac{(\gamma+1) M_R^2}{(\gamma-1) M_R^2 + 2}$$

where the subscript 5 denotes conditions just downstream of the reflected shock wave. Using these relations, the conditions behind a reflected shock wave T_5, p_5, ρ_5 are easily calculated (also tables by Mueller, NACA TN 4063, can be used).

Equilibrium Conditions

As the gases behind the reflected shock wave begin to ionize, the equilibrium conditions will be reached after a certain ionization relaxation time. To calculate the equilibrium conditions, the Saha

equation is used in addition to the normal shock wave jump conditions. It is convenient to use the Mollier chart and the following set of equations. For incident shock waves:

$$\frac{p_2}{p_1} = 1 + \gamma M_s^2 \left(1 - \frac{1}{\eta}\right)$$

$$\frac{h_2}{h_1} = 1 + \frac{\gamma-1}{2} M_s^2 \left(1 - \frac{1}{\eta^2}\right)$$

$$\frac{U_2}{a_1} = M_s \left(1 - \frac{1}{\eta^2}\right)$$

$$\eta = \frac{\rho_2}{\rho_1} = \frac{p_2/p_1}{T_2/T_1} (1 - X_e)$$

For reflected shock waves:

$$\frac{p_5}{p_1} = 1 + \gamma M_s^2 \frac{(\eta-1)(\xi-1)}{(\xi-\eta)}$$

$$\frac{h_5}{h_1} = 1 + (\gamma-1) M_s^2 \frac{(\eta-1)(\xi-1)}{\eta(\xi-\eta)}$$

$$\frac{U_R}{C_s} = \frac{\eta - 1}{\xi - \eta}$$

$$\xi = \frac{\rho_5}{\rho_1} = \frac{p_5/p_1}{T_5/T_1} (1 - X_e)$$

where X_e is the degree of ionization.

The Saha equation for the reaction

$$A \rightleftharpoons A^+ + e$$

is

$$\frac{X_A^2}{(1-X_A^2)} = .65 \times 10^{-6} \frac{T^{5/2}}{p} e^{-E/kT} \frac{Q(A^+)}{Q(A)}$$

where

$$X_A = \frac{n_A^+}{n_A + n_A^+}$$

T in oK, ρ in atm

Q = the position function

E = the ionization potential

For gas mixtures

$$A \rightleftharpoons A^+ + e$$

$$B \rightleftharpoons B^+ + e$$

The Saha equations are

$$\frac{X_A X_e}{(1-X_A)(1-X_e)} = .65 \times 10^{-6} \frac{T^{5/2}}{p} e^{-E_A/kT} \frac{Q(A^+)}{Q(A)}$$

$$\frac{X_B X_e}{(1-X_B)(1-X_e)} = .65 \times 10^{-6} \frac{T^{5/2}}{p} e^{-E_B/kT} \frac{Q(B^+)}{Q(B)}$$

where

$$X_A = \frac{n_A^+}{n_A^+ + n_A}$$

$$X_B = \frac{n_B^+}{n_B^+ + n_B}$$

$$Xe = \frac{n_A^+ + n_B^+}{n_A^+ + n_A + n_B^+ + n_B}$$

Q's = partition functions

The partition functions for various gases are:

$$Q(A^+) = 4 + 2\,e^{-2060/T} + 2\,e^{-15620/T} + \ldots$$

$$Q(A) = 1 + 12\,e^{-13500/T} + \ldots$$

$$Q(Xe^+) = 4 + 2\,e^{-15200/T} + 2\,e^{131,000/T} + \ldots$$

$$Q(Xe) = 1 + 8\,e^{-96500/T} + \ldots$$

$$Q(H^+) = 1$$

$$Q(H) = 2 + 8\,e^{-119,000/T} + 18\,e^{-140,000/T} + \ldots$$

$$Q(O^+) = 4 + 10\,e^{-38600/T} + 6\,e^{-58200/T} + \ldots$$

$$Q(O) = 5 + 3\,e^{-228/T} + e^{-326/T} + 5\,e^{-22800/T} + e^{-48600/T} + \ldots$$

APPENDIX B

LIFETIME OF METASTABLE STATES

The metastable state of an atom is the excited state which, due to the J selection rules, cannot jump to a lower energy state by electric-dipole radiation. The atom must therefore stay in this state until it can give up its energy to another body by collision. Note that is also can decay to a lower energy state by electric-quadrupole or magnetic-dipole radiation with an inherently long lifetime (Phelps 1953).

For most gases the lifetime of the excited state (decay by electric-dipole transition) is of the order of 10^{-8} sec. For the metastable state, the lifetime depends on the energy difference between levels and the wave functions. Usually it is too complicated to calculate, but a rough estimation shows that the transition probability for the electric-quadrupole is of the order of 10^{-8} times the electric-dipole transition probability. Likewise the magnetic-dipole transition probability is of order of 10^{-13} times the electric-dipole transition probability.

More specifically, the lifetimes of a few excited states in hydrogen have been calculated by Breit and Teller (1940). The first excited state of the hydrogen atom is the $2P_{\frac{1}{2}}$ -state. Its lifetime is 1.6×10^{-9} sec. The next excited state is the metastable $2S_{\frac{1}{2}}$ -state. The spontaneous transitions from the 2S-state to the 2P-state have a negligibly small probability, due to the small energy difference. The electric-dipole transitions to the ground state are strictly forbidden (parity rule). The electric-quadrupole transitions are

forbidden (both states $\ell = 0$). The magnetic-dipole transitions from 2S to 1S are not strictly forbidden, but their probability is smaller than those for allowed electric-dipole transitions by a factor of 10^{-13}. The largest probability for a 2S-1S transition comes from the simultaneous emission of two photons whose combined energies equal the energy difference between the two atomic states. The mean lifetime due to this transition has been calculated by Breit and Teller (1940) to be about 1/7 sec.

The effect of an electric field on the lifetime of the metastable state in hydrogen is discussed by Bethe and Salpeter (1957). Due to the electric field the 2S-state is mixed with the 2P-state which gives a mean lifetime of

$$\tau(E) = \left(\frac{E}{475\ \text{v/cm}}\right)^{-2} \tau_p$$

where τ_p = lifetime of 2P-state = 1.6×10^{-9} sec. For an electric field of 4 volts/cm (this corresponds to an ion density of 3×10^{12} ions/cm^3) the lifetime of the 2S-state is about 6 μsec.

REFERENCES

1. Bates, D. R. 1962 Atomic and Molecular Processes, p. 605 (ed. D. R. Bates). New York and London: Academic Press.

2. Benson, S. W. 1960 The Foundation of Chemical Kinetics. New York: McGraw Hill.

3. Bethe, H. A. and Salpeter, E. E. 1957 Quantum Mechanics of One- and Two-Electron. New York: Academic Press.

4. Bradley, J. N. and Kistiakowsky, G. B. 1961 J. Chem Phys. 35, 256.

5. Breit, G. and Teller, E. 1940 Astrophys. J. 91, 215.

6. Chapman, S. and Cowling, T. G. 1952 The Mathematical Theory of Non-Uniform Gases, Chapter V. London: Cambridge University Press.

7. Creswell, R; DiValentin, M. A. and Dove, J. E. 1966, Phys. Fluid 9, 2285.

8. Dove, J. E. and Moulton, D. Mcl. 1965 Proc. Roy. Soc. A283, 216.

9. Goldsworthy, F. A. 1958 J. Fluid Mech. 5, 164.

10. Harwell, K. E. and Jahn, R. G. 1964 Phys. Fluids 7, 214: Ibid 1554.

11. Hasted, J. B. 1962 Atomic and Molecular Processes, p. 715 (ed. D. R. Bates). New York and London: Academic Press.

12. Hasted, J. B. 1964 Physics of Atomic Collisions. Washington: Butterworths.

13. Hirschfelder, J. O.; Curtiss, C. F. and Bird, R. B. 1954 Molecular Theory of Gases and Liquids. New York: John Wiley and Sons Inc.

14. Jahn, R. G. and Weimer, D. 1958 J. Appl. Phys. 29, 741.

15. Kelly, A. J. 1966 J. Chem. Phys. 45, 1723.

16. Klein, A. 1967 Ph. D. Thesis, Caltech.

17. Liepmann, H. W.; Roshko, A.; Coles, D. and Sturtevant, B. 1962 Rev. Sci. Instr. 33, 625.

REFERENCES (Cont.)

18. Liepmann, H. W. and Roshko, A. 1957 Elements of Gasdynamics. New York and London: John Wiley and Sons Inc.

19. Massey, H. S. W. and Burhop, H. S. 1952 Electronic and Ionic Impact Phenomena. Oxford: Clarendon.

20. Nier, A. O. 1947 Rev. Sci. Instr. 18, 398.

21. Petschek, A. and Byron, S. 1957 Ann. Phys. (N. Y.) 1, 270.

22. Phelps, A. V. 1953 Phys. Rev. 89, 1202.

23. Phelps, A. V. 1958 Phys. Rev. 110, 1362.

24. Roshko, A. 1960 Phys. Fluids 3, 835.

25. Sturtevant, B. 1961 Phys. Fluids 4, 1064.

26. Sturtevant, B. 1966 J. Fluid Mech. 25, 641.

27. Sturtevant, B. and Slachmuylders, E. 1964 Phys. Fluids 7, 1201.

28. Su, C. H. 1965 AIAA J. 3, 842.

29. Weymann, H. D. 1958 University of Maryland Tech. Note BN-144.

TABLE 1

TEST CONDITIONS AND TRANSPORT PARAMETERS FOR TYPICAL EXPERIMENTS IN ARGON AND XENON

Gases	Argon	Xenon
p_1 (μHg.)	180	100
T_1 (^oK)	300	300
n_1 (cm^{-3})	6.4×10^{15}	3.5×10^{15}
M_s	7.3	8.8
T_5 (^oK)	12,000	17,500
p_5 (mmHg.)	66.5	55.5
n_5 (cm^{-3})	5.86×10^{16}	3.34×10^{16}
μ_5 (g/cm/sec)	35.5×10^{-4}	46.6×10^{-4}
ν_5 (cm^2/sec)	9.1×10^{2}	6.4×10^{2}
D_5 (cm^2/sec)	1.5×10^{3}	1.0×10^{3}
$D_{5\ am}$ (cm^2/sec)	2.8×10^{2}	2.2×10^{2}
$\bar{C}_5$ (cm/sec)	2.5×10^{5}	1.67×10^{5}
π_5 (cm)	2×10^{-2}	2×10^{-2}
λ_5 at wall (cm)	8×10^{-5}	9.6×10^{-5}
λ_1 (cm)	3×10^{-2}	5.3×10^{-2}
μ_5^+ (cm^2/v/sec)	1.4×10^{3}	6.7×10^{2}
Sampling orifice dia. (cm)	0.015	0.015
End wall thermal layer at 100 μsec (cm)	1	0.8

TABLE 1 (Cont.)

TEST CONDITIONS AND TRANSPORT PARAMETERS FOR TYPICAL EXPERIMENTS IN ARGON AND XENON

Gases	Argon	Xenon
Test time (μsec)	380	450
Equlibrium conditions T_5 (^{o}K)	9, 100	8, 000
p_5 (mmHg)	61.6	46
Degree of ionization α	0.027	0.094

TABLE 2

PARTITION FUNCTION CONSTANTS FOR

A, Kr, Xe, H, O and e^-

Particle	Mass M amu	Electron Degenercy g_n	Electron Energy E_n/k ^oK	Ionization Energy E_I/k ^oK
A	40	1	0	183, 000
		12	135, 000	
A^+	40	4	0	321, 000
		2	2, 060	
		2	156, 200	
Kr	83.7	1	0	162, 500
		8	116, 000	
Kr^+	83.7	4	0	285, 000
		2	7, 700	
		2	157, 000	
Xe	131.3	1	0	141, 000
		8	96, 500	
Xe^+	131.3	4	0	246, 000
		2	15, 200	
		2	131, 000	
H	1	2	0	157, 800
		8	119, 000	
		18	140, 000	
H^+	1	1	0	0
O	16	5	0	157, 800
		3	228	
		1	326	
		5	22, 800	
		1	48, 600	
O^+	16	4	0	408, 000
		10	38, 600	
		6	58, 200	
e^-	1/1820	2	0	0

TABLE 3

RELATIVE ABUNDANCE OF IMPURITY IONS IN

DIFFERENT SERIES OF RUNS IN "PURE" ARGON

Mass M amu	Ion	Series 1 p_1=30μHg T_5=16, 000°K n_I/n_A=300ppm	Series 2 p_1=30μHg T_5=16, 000°K n_I/n_A=300ppm	Series 3 p_1=180μHg T_5=12, 000°K n_I/n_A=50ppm
40	A^+	1	1	1
1	H^+	3.30	3.75	31
2	H_2^+	0	---	---
12	C^+	---	0.38	---
12, 13		0.60	---	---
14	N^+	0.38	0.10	---
15	NH^+	0	0.18	---
16	O^+	5.50	1.30	13
17	OH^+	---	---	0.03
18	H_2O^+	---	0.02	---
18, 19		0.15	---	---
20	A^{++}	---	0.02	---
23	Na^+	---	---	1.16
26, 27, 28		1.25	---	---
28	N_2^+	---	0.01	---
32	O_2^+	0.50	---	---
39	K^+	---	---	0.2
41	AH^+	---	---	2.3
44	CO_2^+	0	---	---
80	A_2^+	0	0	---

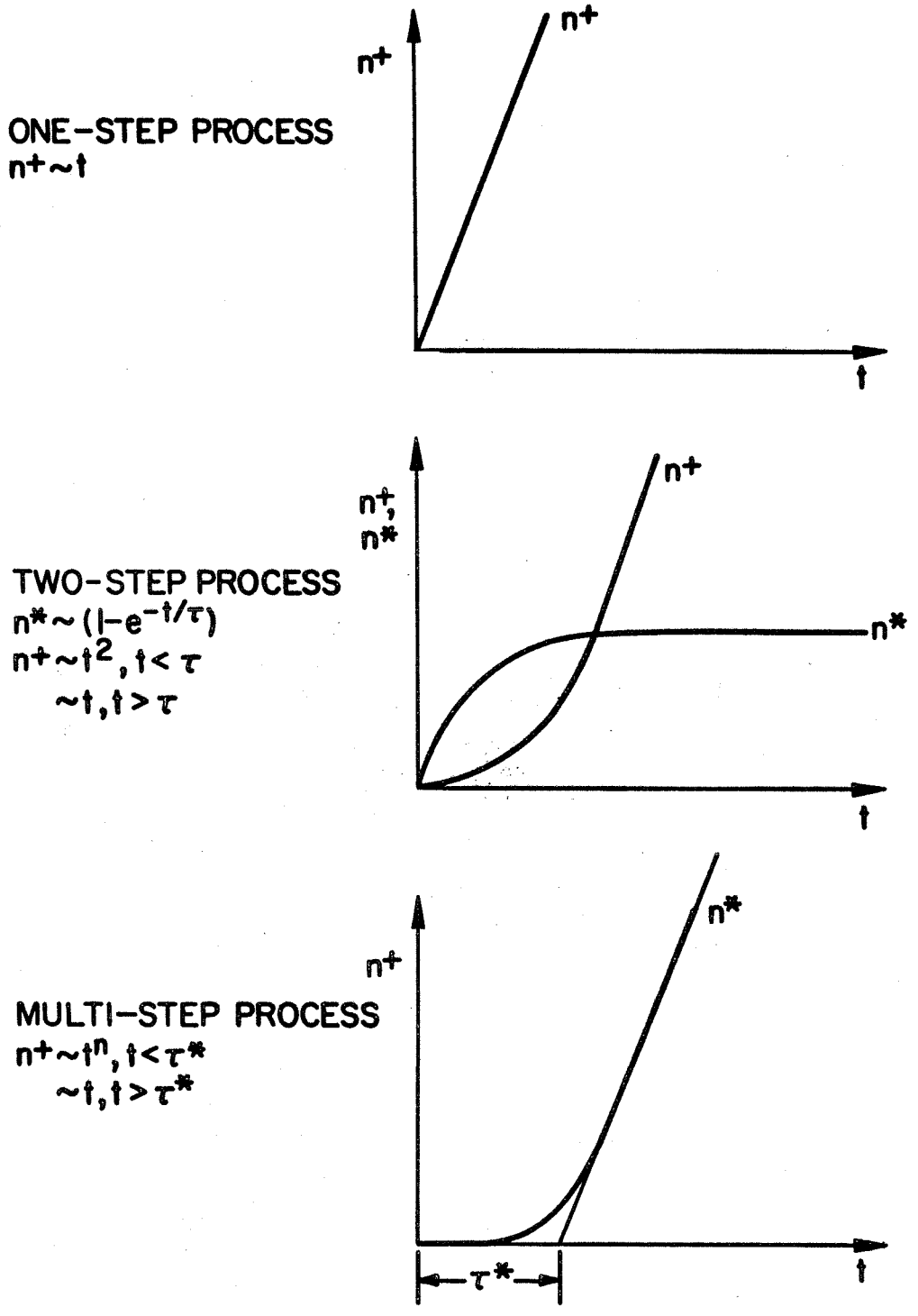

Figure 1. Plot of ion density against time for one-step, two-step and multi-step reactions.

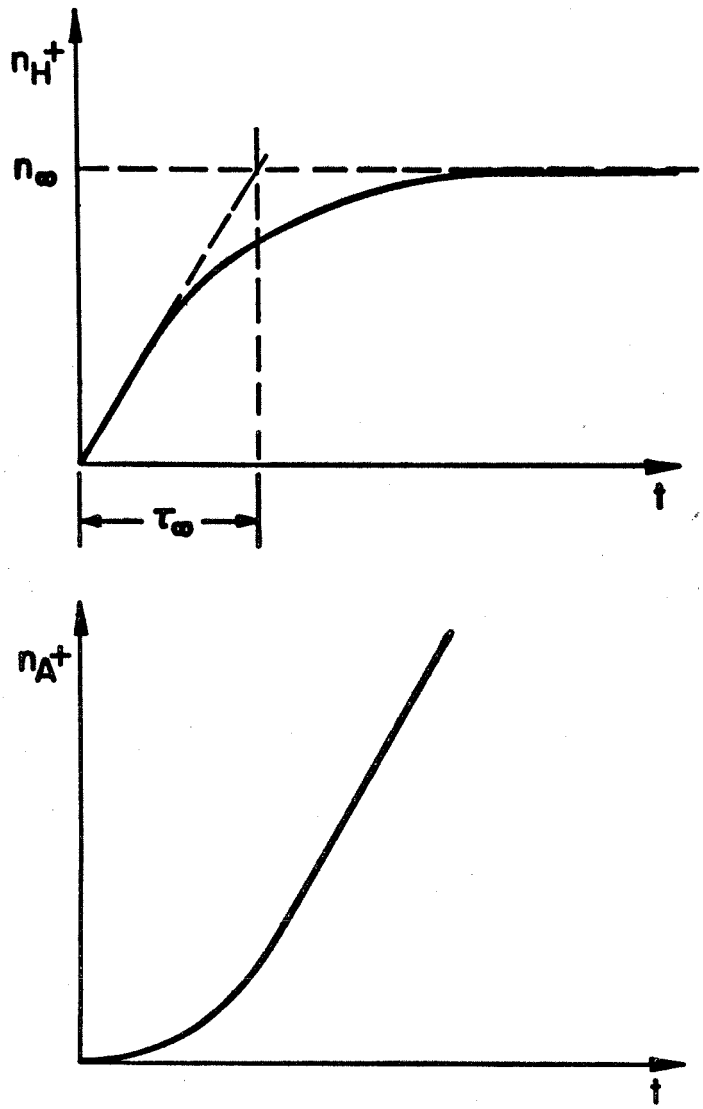

$$n_H^+ = \frac{n_\infty \tanh t/\tau_\infty}{1 - \frac{B\tau_\infty}{2}(1-\tanh t/\tau_\infty)} \quad , \quad n_\infty = \frac{2A}{\sqrt{B^2+4AC}+B}$$

$$n_A^+ = Dt + E\int n_H^+ dt \qquad \tau_\infty = \frac{2}{\sqrt{B^2+4AC}+B}$$

Figure 2. Plot of ion density against time for a gas mixture.

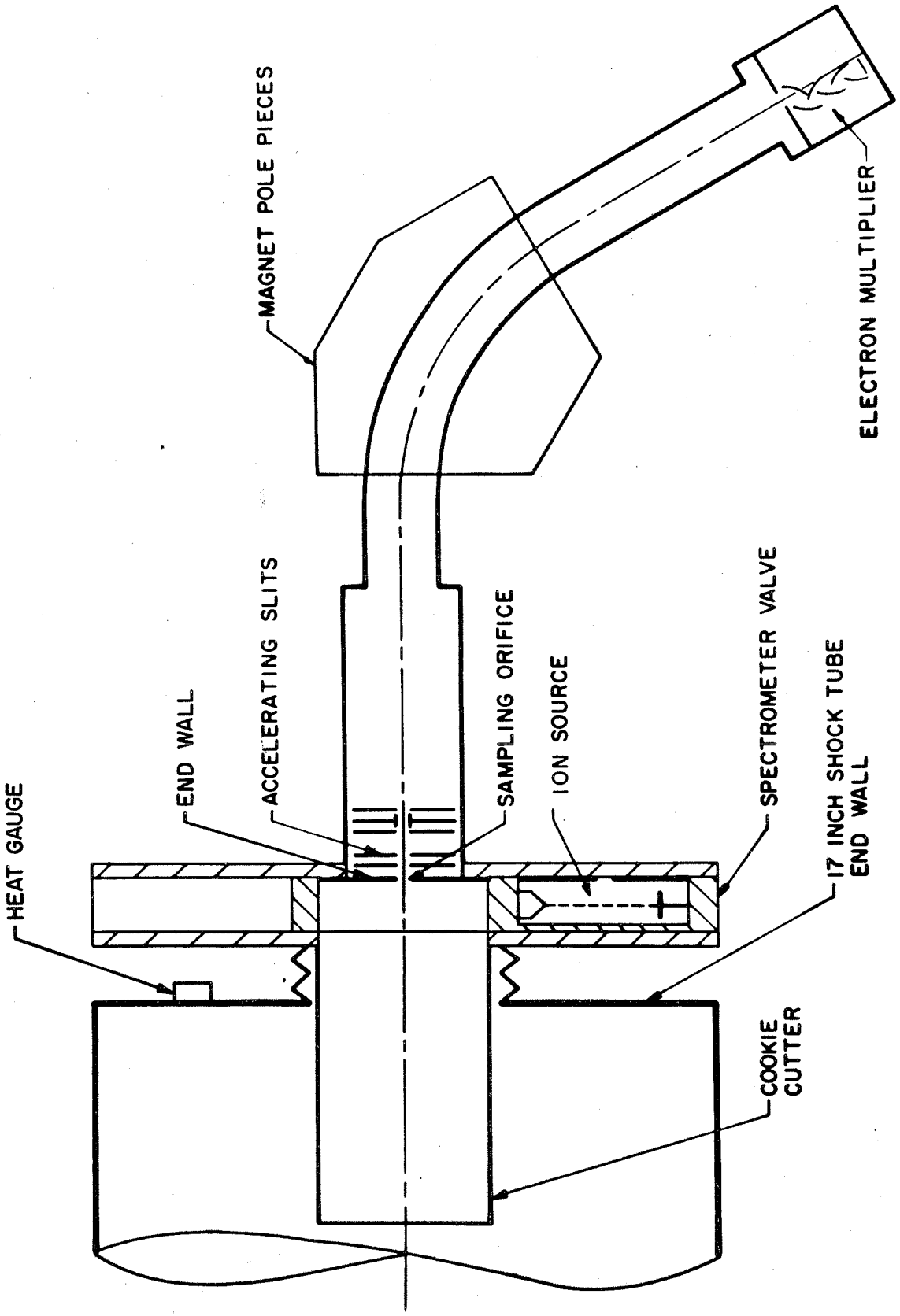

Figure 3. Mass spectrometer installation.

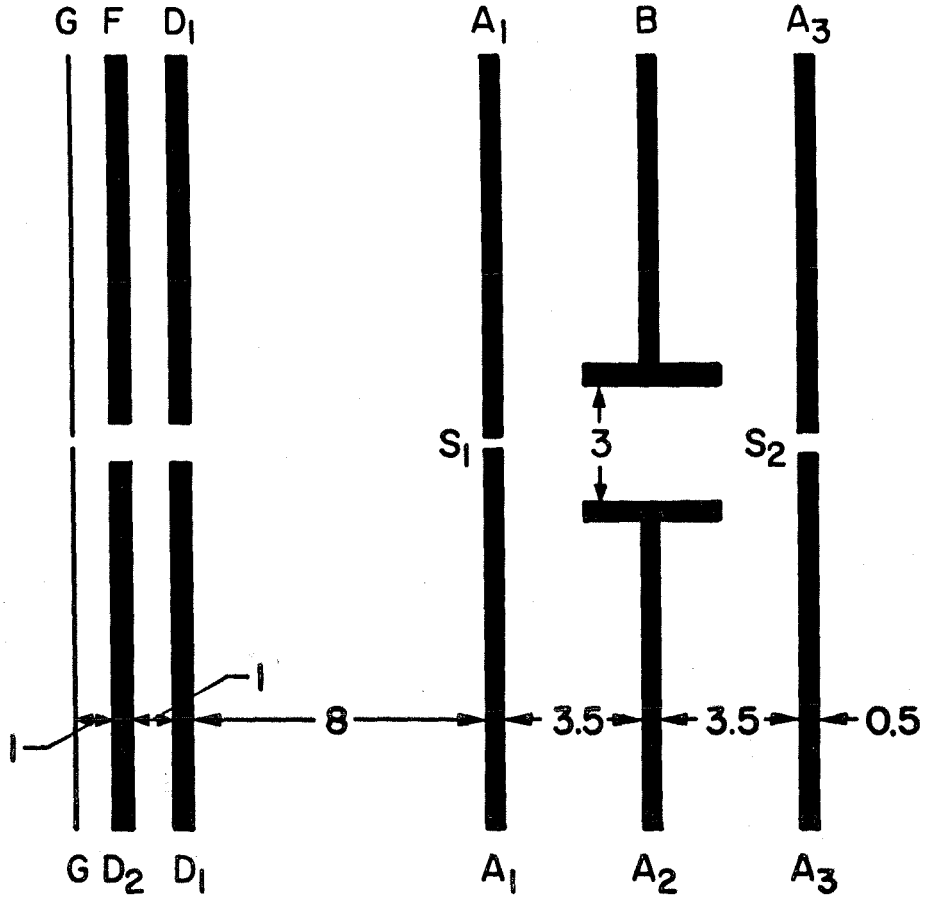

G : End wall, orifice = 0.15 dia.

D_2, F : Focus plates, 2 half-plates separated by 1 mm.

D_1 : Drawout plate, slit: 1 × 15

A_1, A_3 : Accelerating plates, slits: S_1 = 0.25 × 15, S_2 = 0.5 × 15

A_2, B : Deflecting plates, 2 T-shaped plates

All dimensions in mm.

Figure 4. Arrangement of accelerating slits.

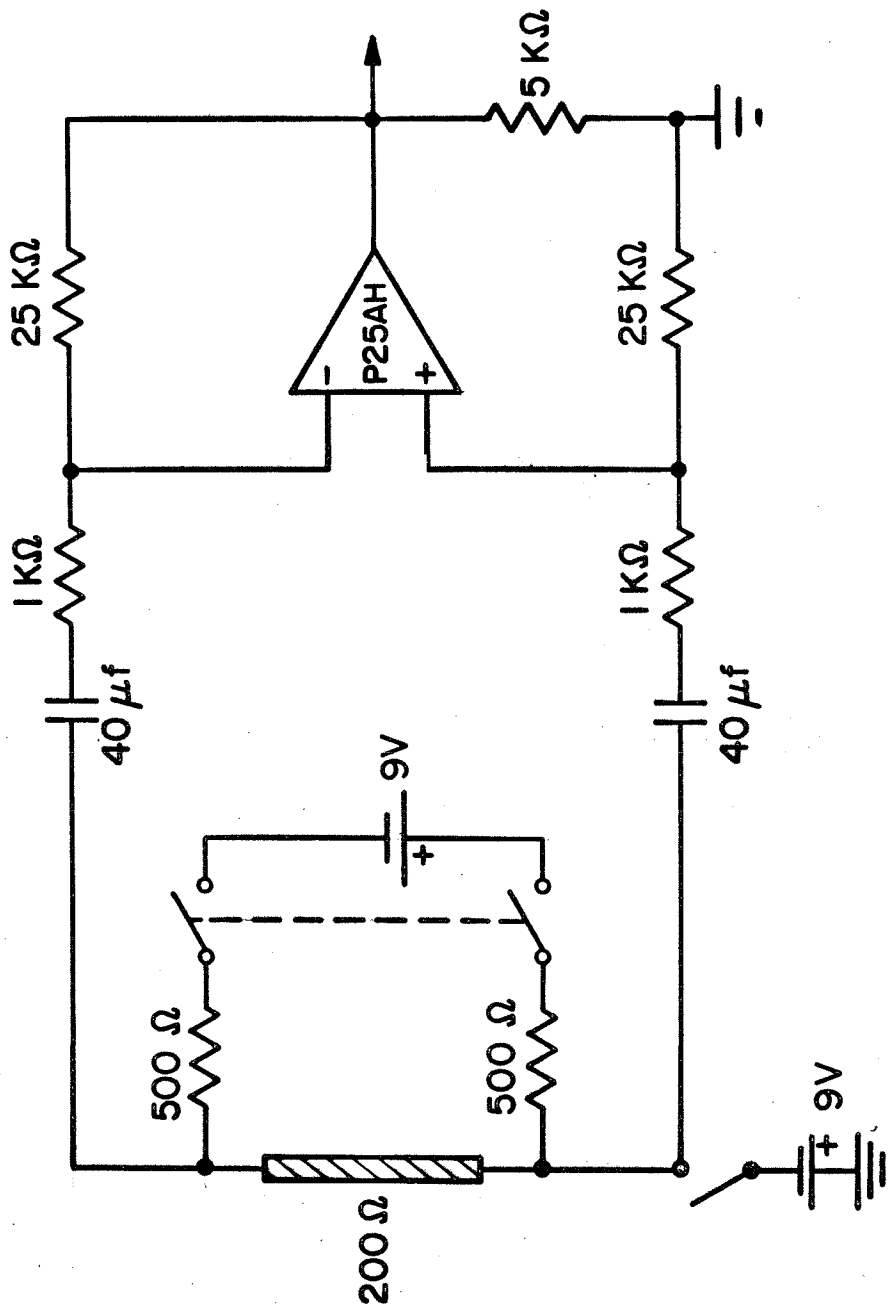

Figure 5. Heat gauge circuit.

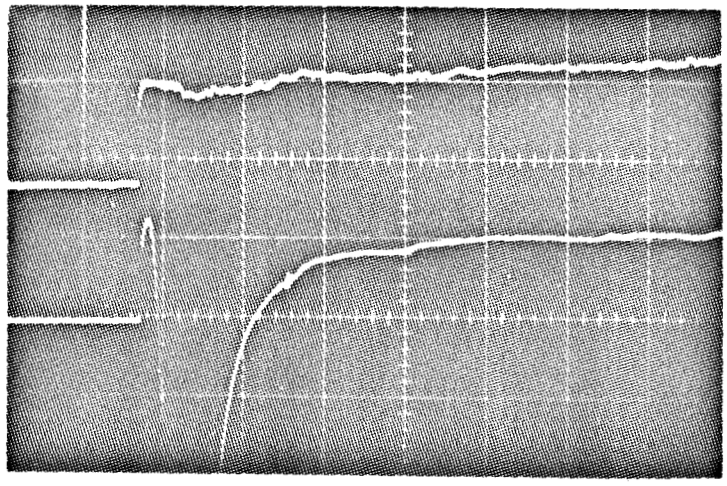

End wall heat gauge output in argon
Upper trace: non-shorting heat gauge
Lower trace: ordinary heat gauge
Sweep rate: 50 μsec/cm
Sensitivity: 100 mv/cm

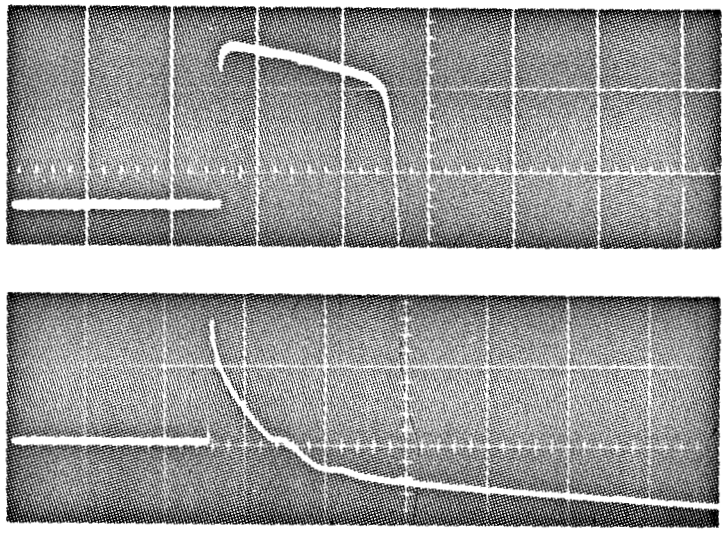

Side wall heat gauge output in xenon
Upper trace: non-shorting heat gauge
Lower trace: ordinary heat gauge
Sweep rate: 100 μsec/cm
Sensitivity: 100 mv/cm

Figure 6. Heat gauge traces using non-shorting and ordinary circuit.

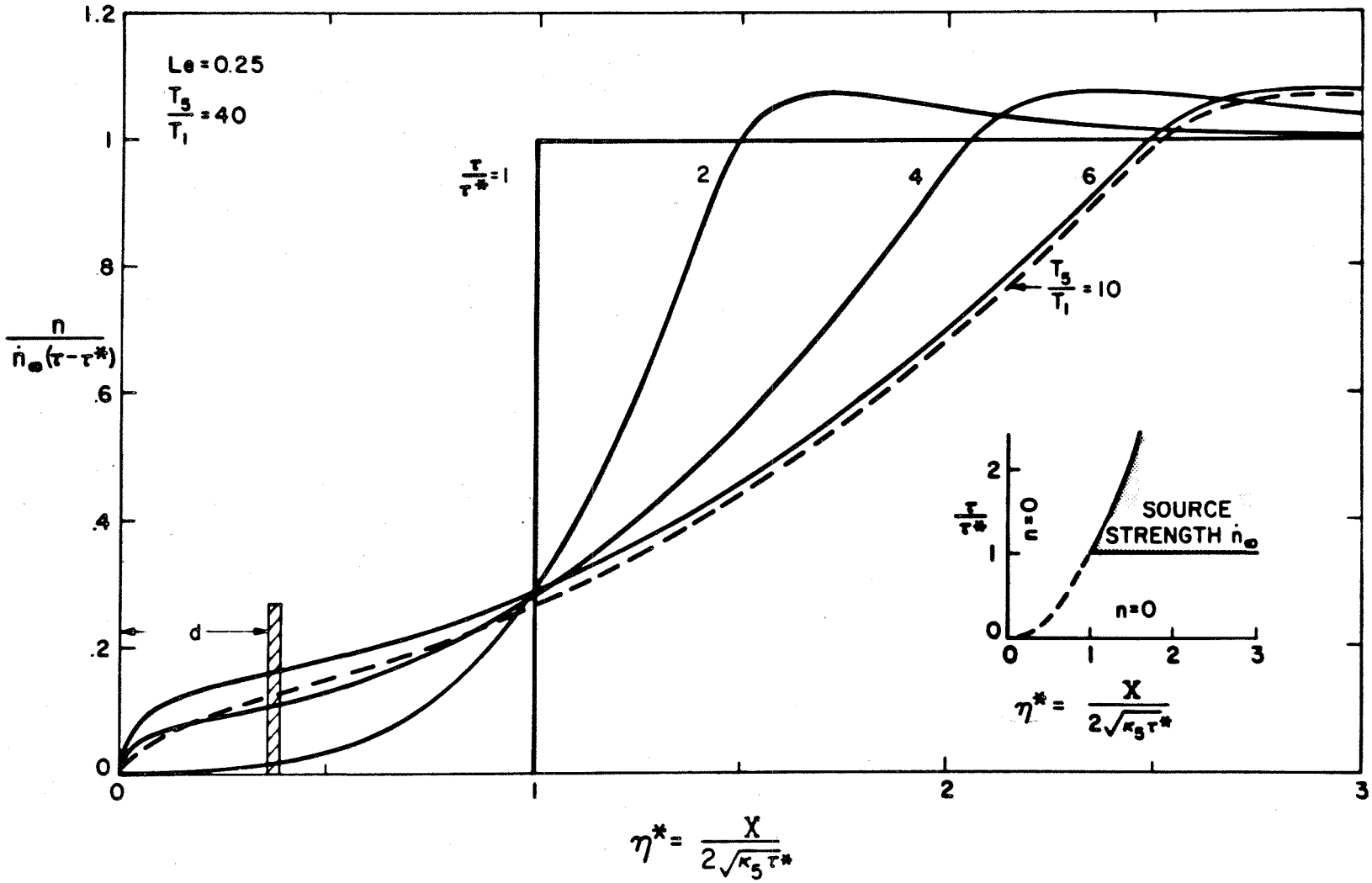

Figure 7. Ion density distribution in thermal layer for Le = 0.25.

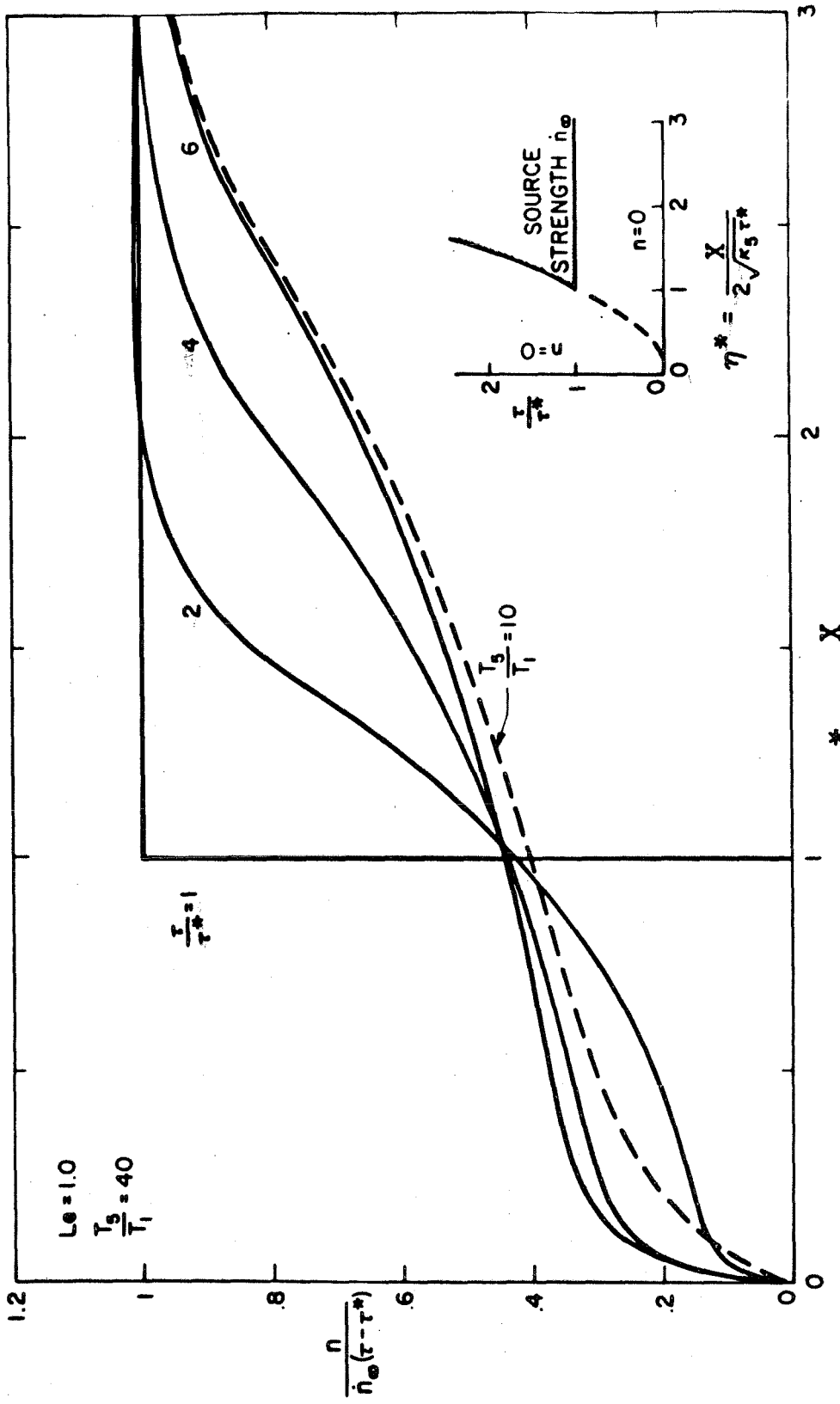

Figure 8. Ion density distribution in thermal layer for Le = 1.

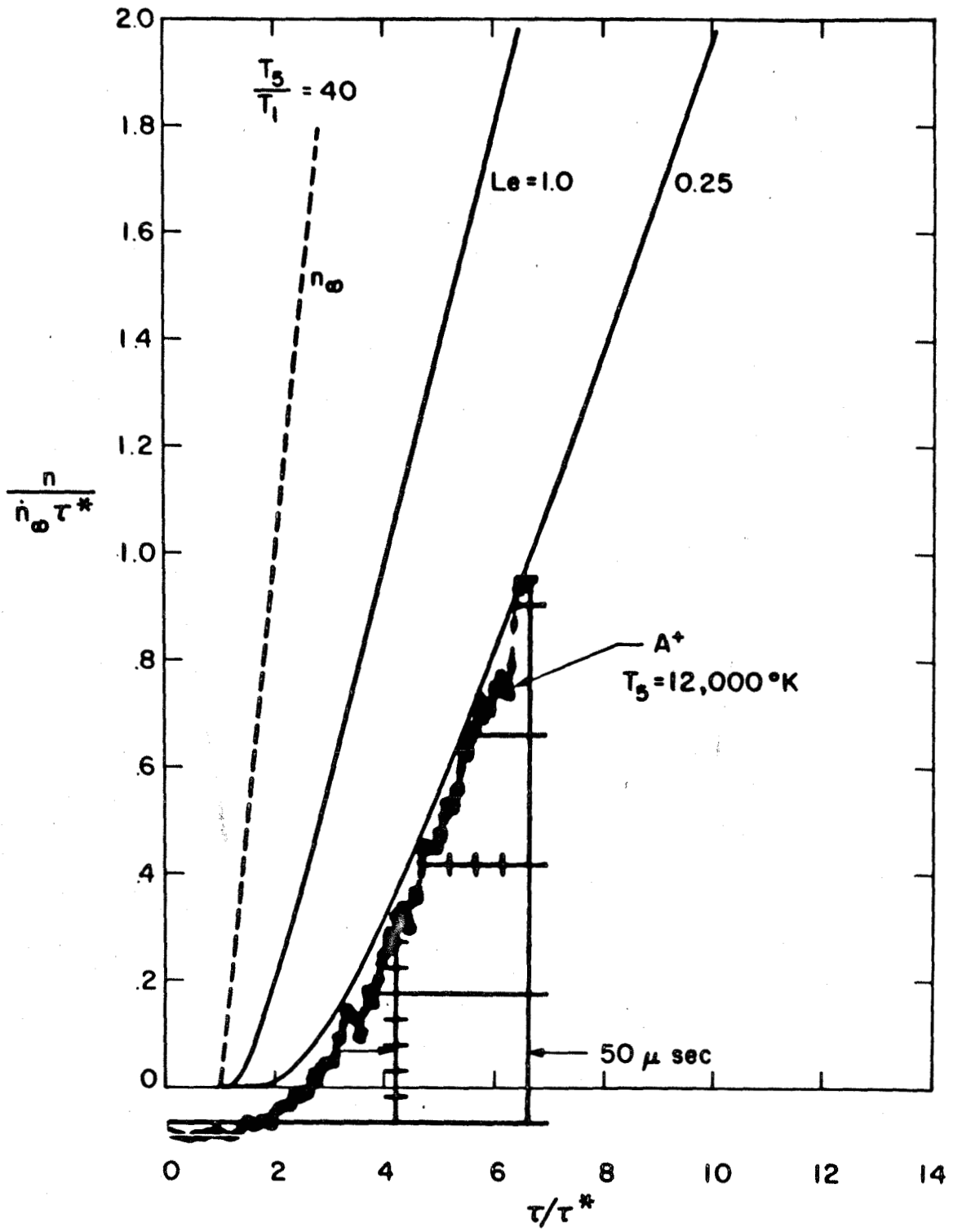

Figure 9. Plot of ion flux through orifice against time.

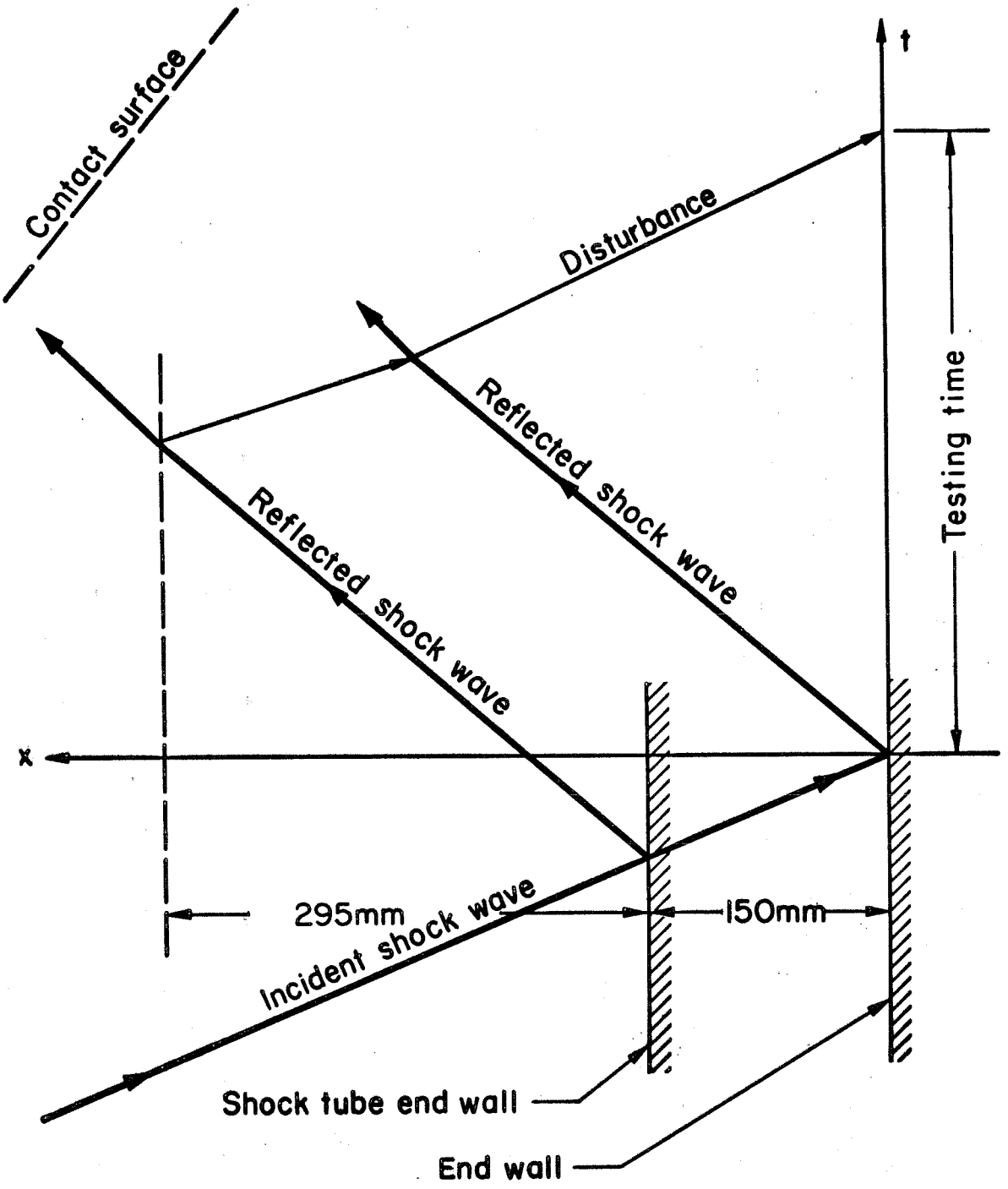

Figure 10. x-t diagram near end wall.

$p_1 = 180 \mu$Hg, $T_5 = 12,000^{\circ}$K, $n_I/n_A = 50$ ppm. Upper trace mass 1 amu, middle trace mass 16 amu, and lower trace mass 40 amu. Sweep rate 100 μ sec per large division, left to right; sensitivity 5×10^{-11} amp per large division. Arrow shows time of shock reflection.

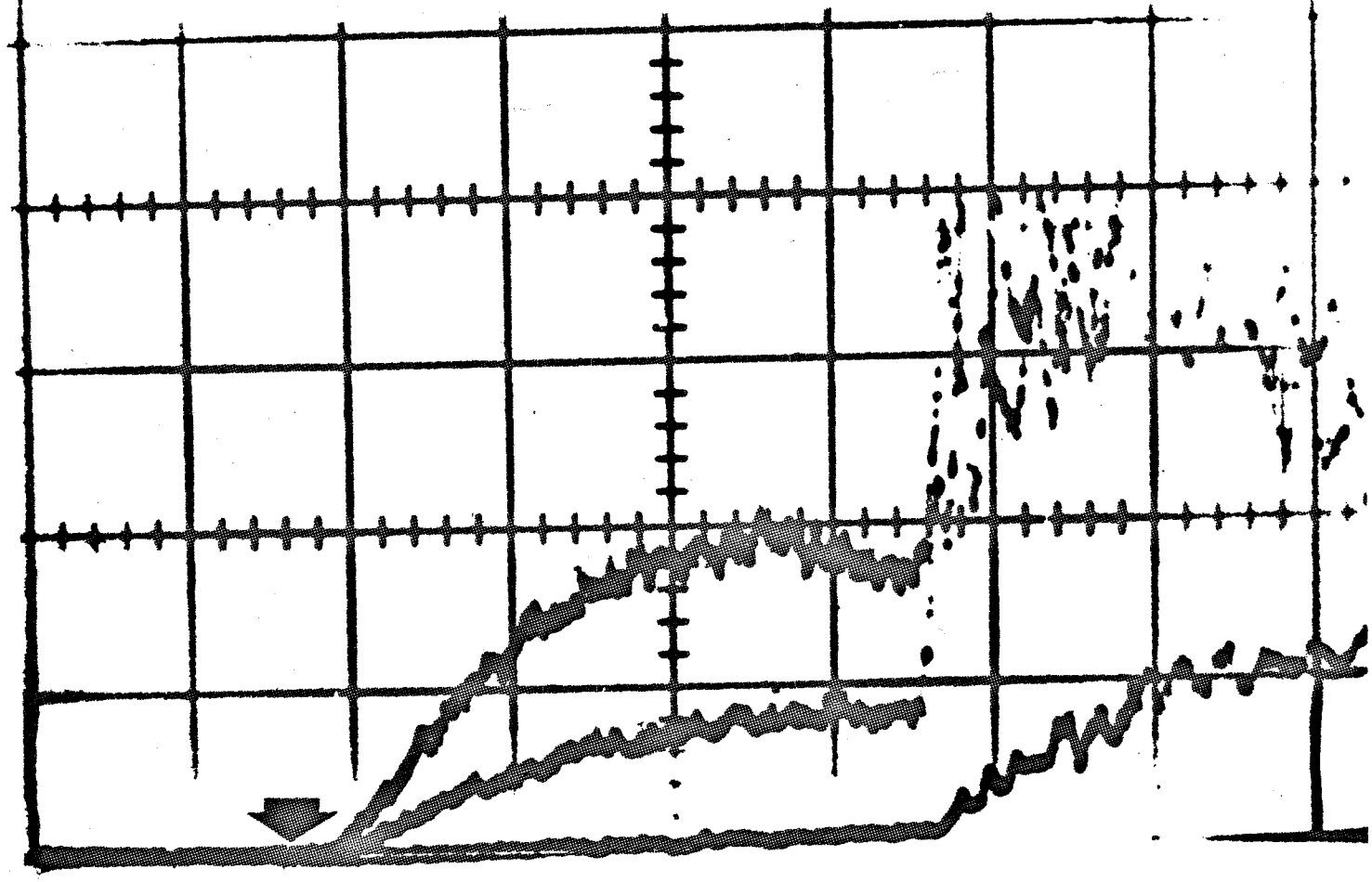

Figure 11. Collector current against time for mass 1, 16, and 40 amu.

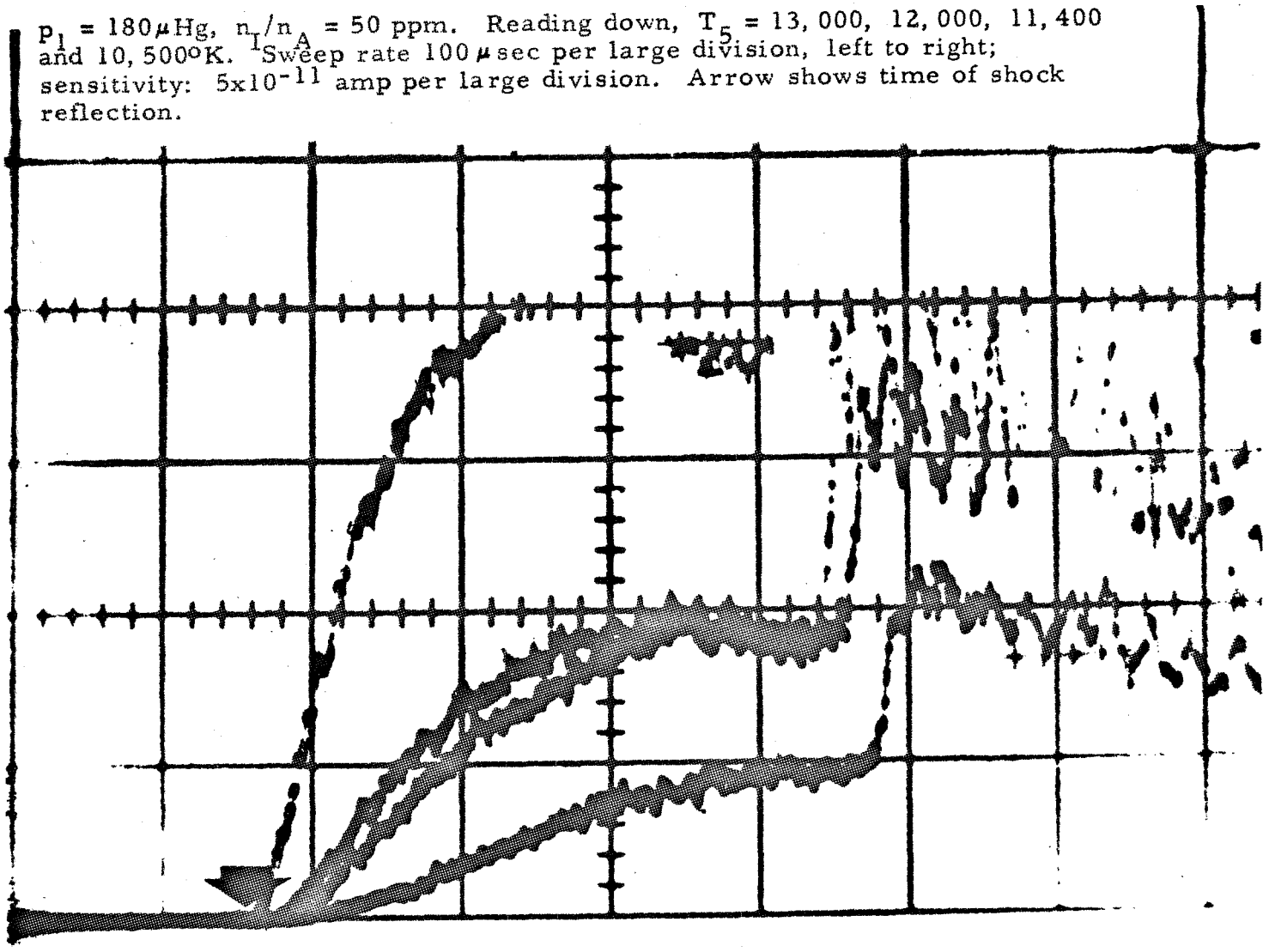

Figure 12. Collector current against time for mass 1 amu at four different temperatures.

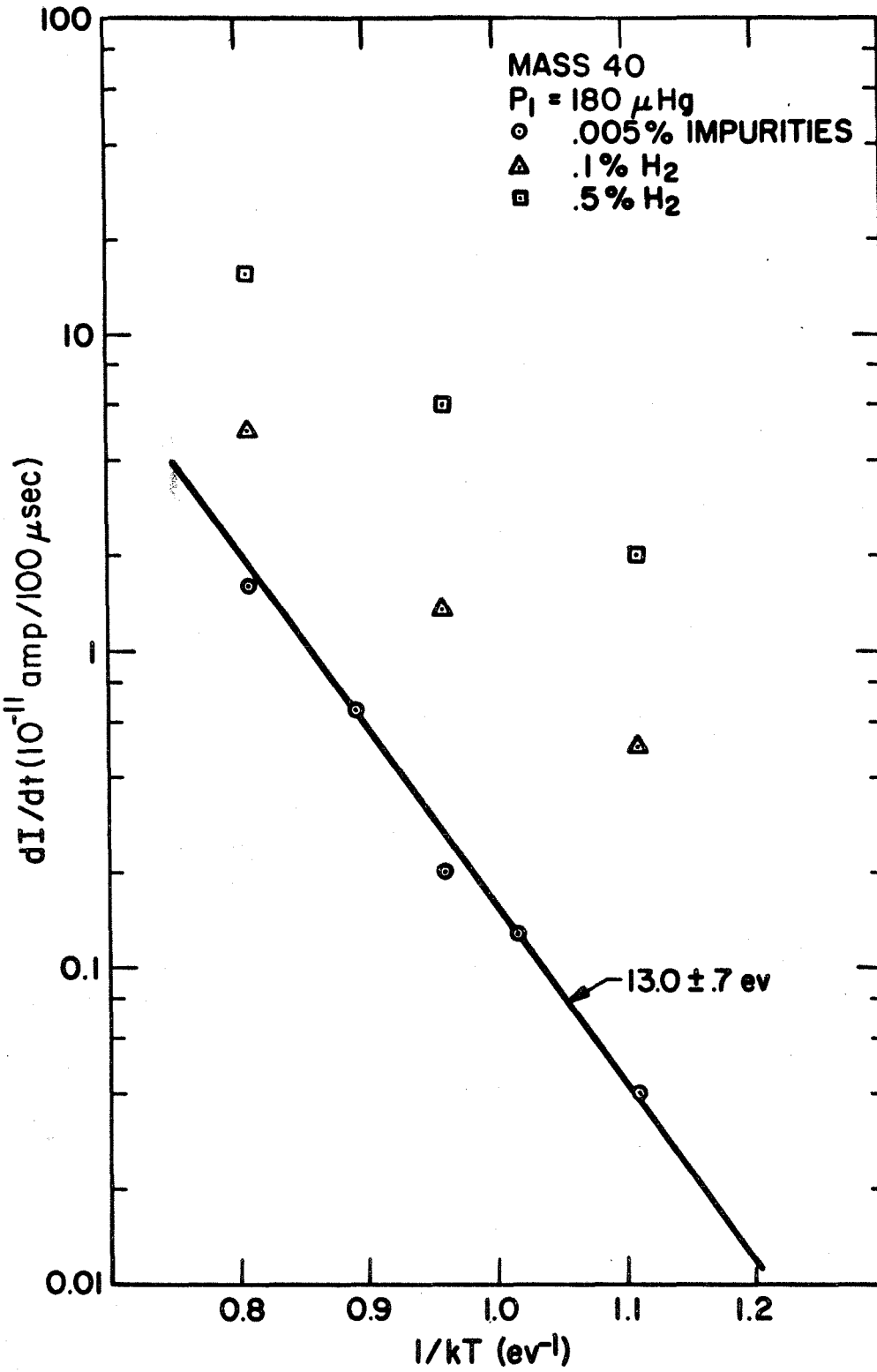

Figure 13. Arrhenius plot of argon ions.

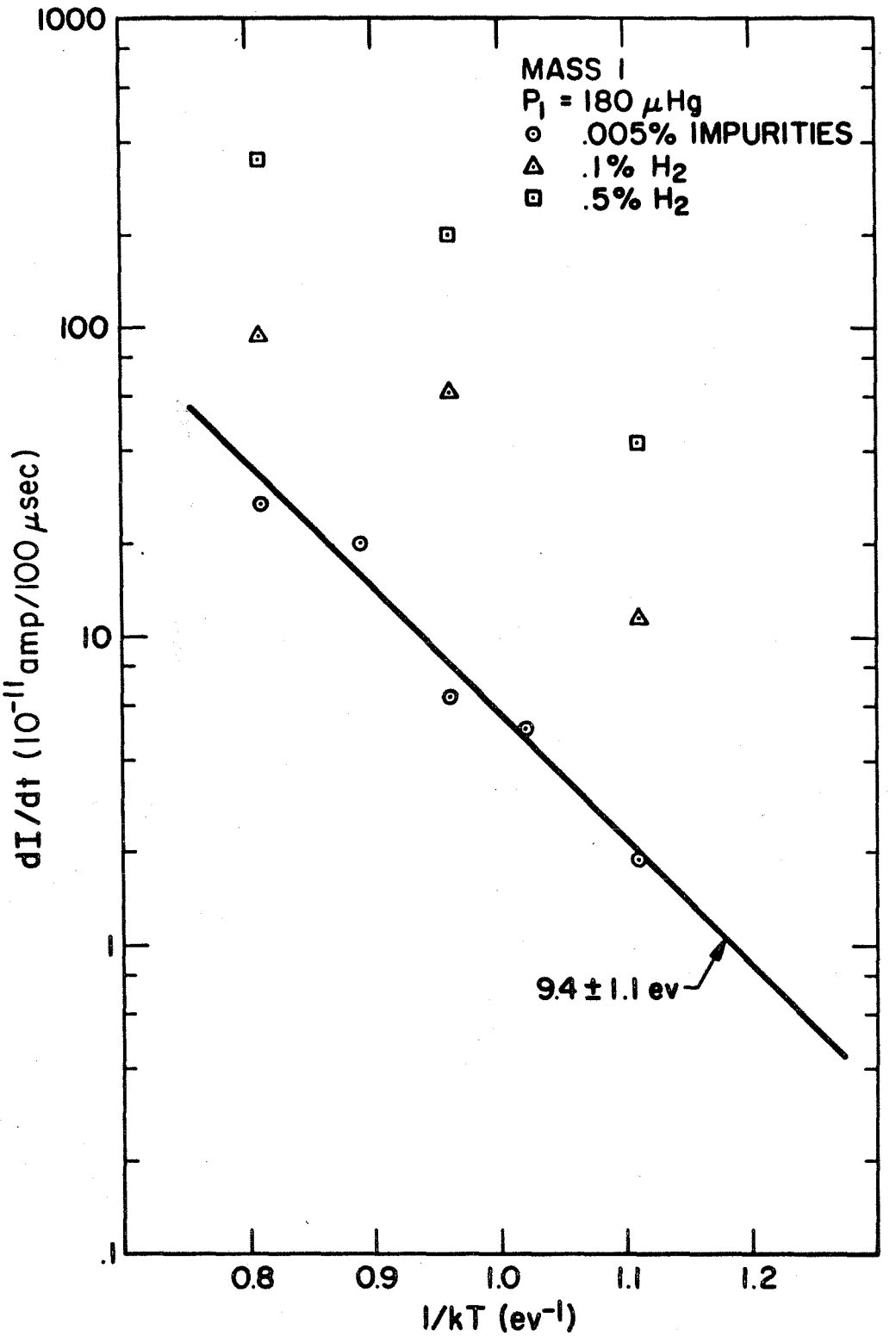

Figure 14. Arrhenius plot of hydrogen ions.

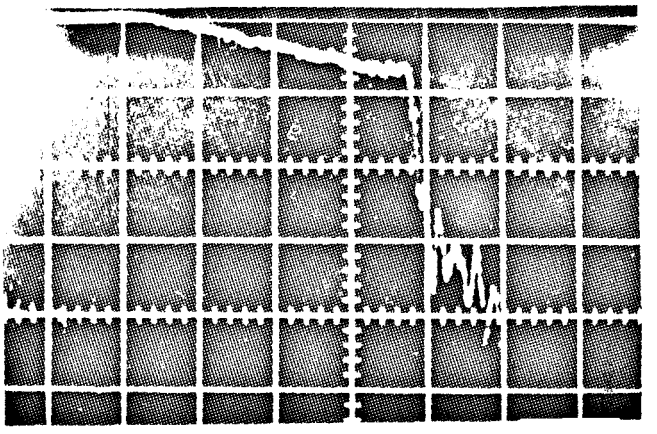

Argon ion trace
p_1 = 180 μHg, T_5 = 12,000°K,
0.1% H_2 in argon
Sweep rate: 100 μsec/cm
Sensitivity: 5×10^{-11} amp/cm

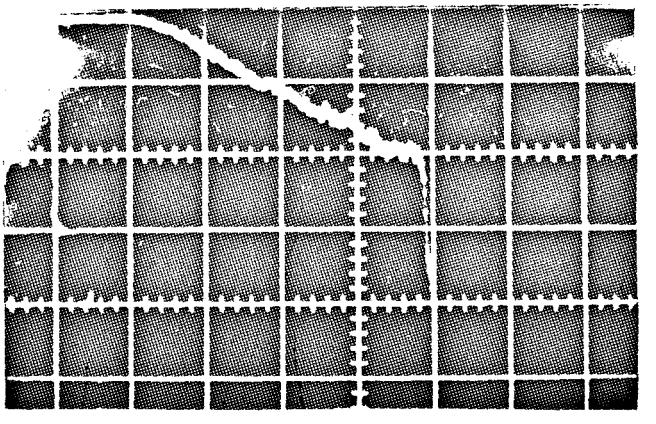

Argon ion trace
p_1 = 180 μHg, T_5 = 12,000°K,
0.5% H_2 in argon
Sweep rate: 100 μsec/cm
Sensitivity: 5×10^{-11} amp/cm

Figure 15. Argon ion traces; 0.1 % H_2 and 0.5 % H_2 added to argon.

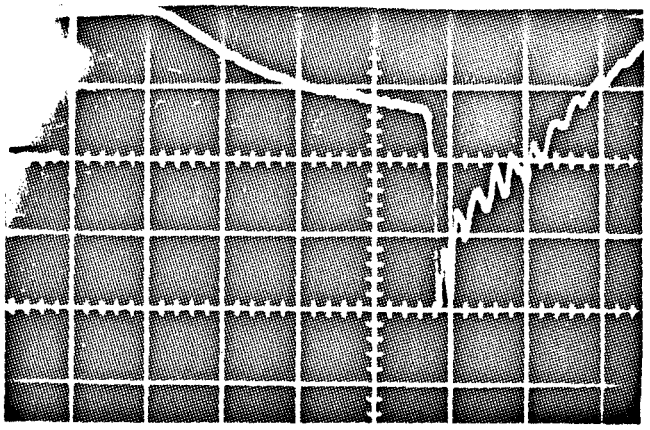

Hydrogen ion trace
p_1 = 180 μHg, T_5 = 12,000°K,
0.1% H_2 in argon
Sweep rate: 100 μsec/cm
Sensitivity: 10^{-9} amp/cm

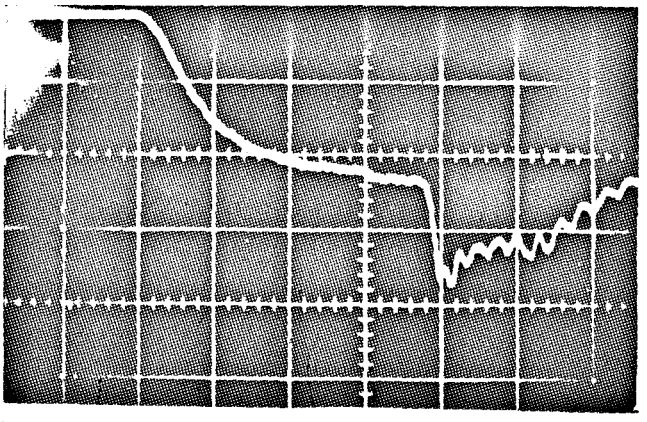

Hydrogen ion trace
p_1 = 180 μHg, T_5 = 12,000°K,
0.5% H_2 in argon
Sweep rate: 100 μsec/cm
Sensitivity: 10^{-9} amp/cm

Figure 16. Hydrogen ion traces in 0.1 % H_2 and 0.5 % H_2 added to argon.

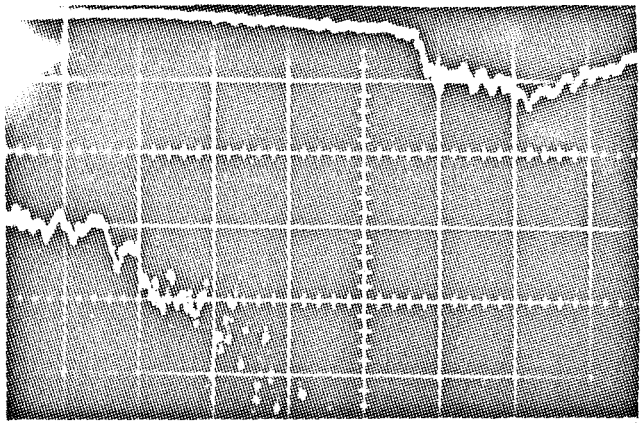

Oxygen ion trace

p_1 = 180 μHg, T_5 = 12,000°K,

0.1% H_2 in argon

Sweep rate: 100 μsec/cm (upper trace)

Sensitivity: 5×10^{-11} amp/cm (upper trace)

Sweep rate: 50 μsec/cm (lower trace)

Sensitivity: 2×10^{-12} amp/cm (lower trace)

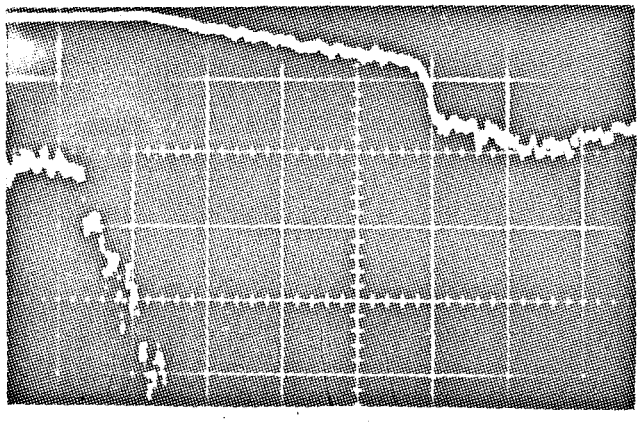

Oxygen ion trace

p_1 = 180 μHg, T_5 = 12,000°K,

0.5% H_2 in argon

Sweep rate: 100 μsec/cm (upper trace)

Sensitivity: 5×10^{-11} amp/cm (upper trace)

Sweep rate: 50 μsec/cm (lower trace)

Sensitivity: 2×10^{-12} amp/cm (lower trace)

Figure 17. Oxygen ion traces; 0.1 % H_2 and 0.5 % H_2 added to argon.

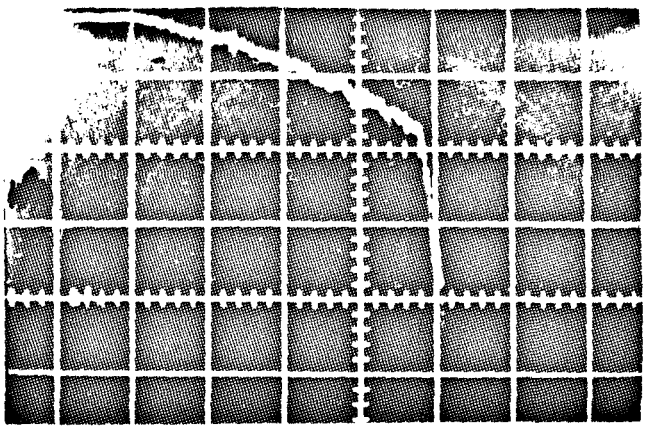

Xenon ion trace
p_1 = 180 μHg, T_5 = 12,000°K,
0.5% Xe in argon
Sweep rate: 100 μsec/cm
Sensitivity: 5×10^{-11} amp/cm

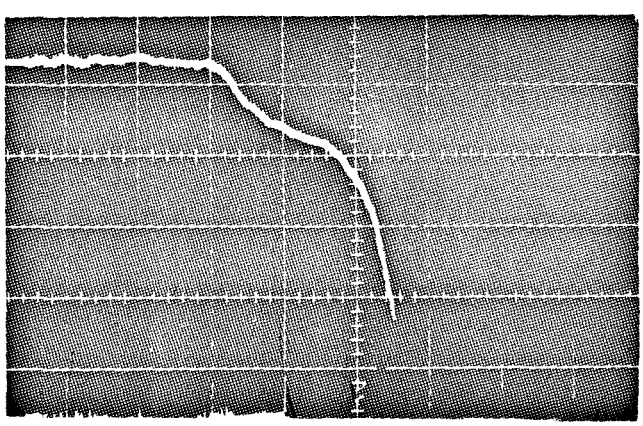

Xenon ion trace
p_1 = 100 μHg, T_5 = 17,500°K,
xenon
Sweep rate: 100 μsec/cm
Sensitivity: 10^{-10} amp/cm

Figure 18. Xenon ion traces.

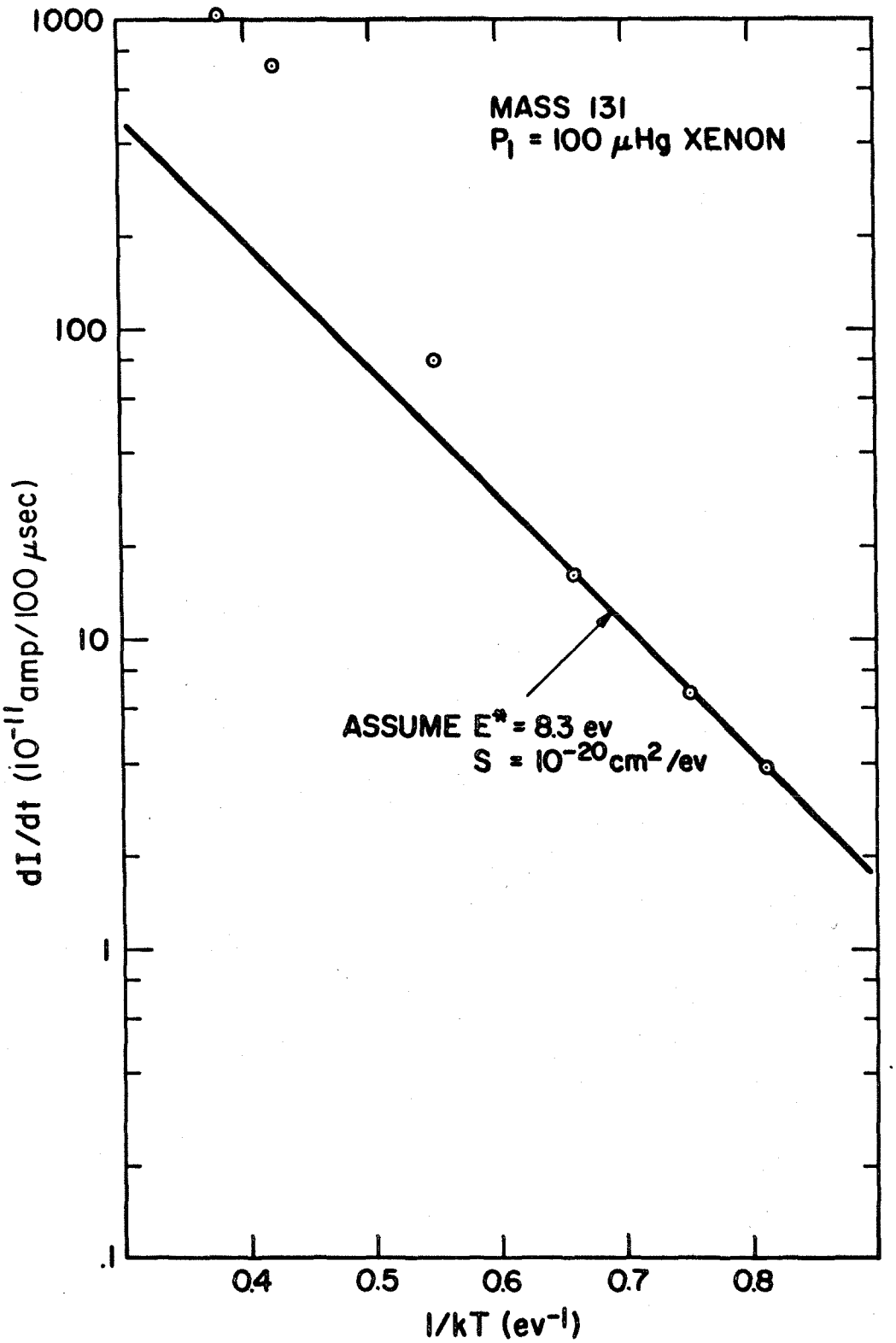

Figure 19. Arrhenius plot of xenon ions.